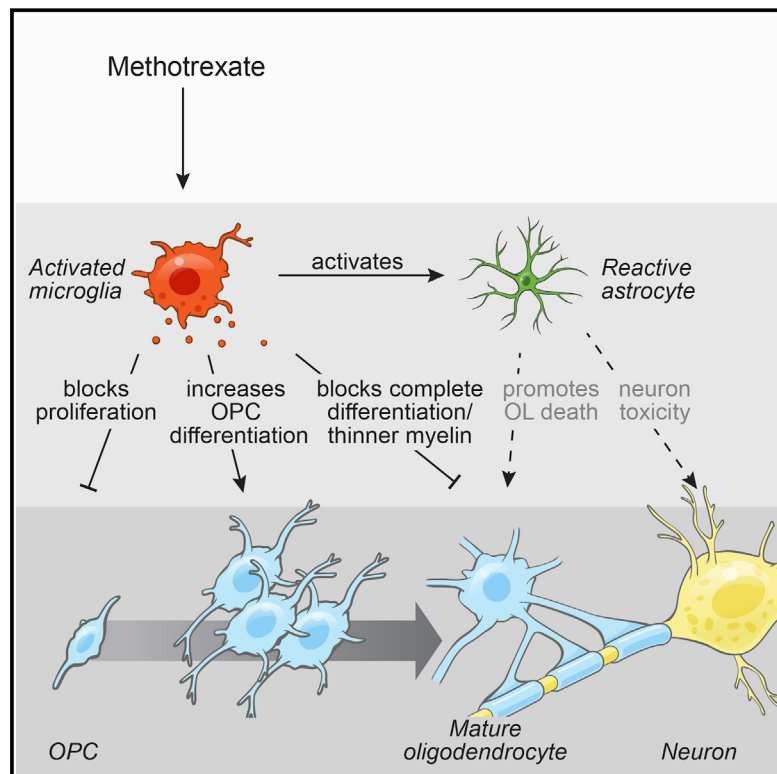


Methotrexate Chemotherapy Induces Persistent Tri-glial Dysregulation that Underlies Chemotherapy-Related Cognitive Impairment

Graphical Abstract



Authors

Erin M. Gibson, Surya Nagaraja,
Alfonso Ocampo, ..., Shane Liddelow,
Hannes Vogel, Michelle Monje

Correspondence

monje@stanford.edu

In Brief

Microglial activation by methotrexate leads to a persistent disruption of oligodendrocyte lineage dynamics and astrocyte reactivity, resulting in the long-term cognitive impairment associated with chemotherapy.

Highlights

- Chemotherapy depletes oligodendrocyte lineage (OL) cells in humans
- Methotrexate chemotherapy disrupts OL dynamics, myelin, and cognition in mice
- Methotrexate induces chronic microglial activation and astrocyte reactivity
- Microglial depletion rescues glial cell dysregulation and cognitive deficits



Methotrexate Chemotherapy Induces Persistent Tri-glial Dysregulation that Underlies Chemotherapy-Related Cognitive Impairment

Erin M. Gibson,¹ Surya Nagaraja,¹ Alfonso Ocampo,¹ Lydia T. Tam,¹ Lauren S. Wood,¹ Praveen N. Pallegar,¹ Jacob J. Greene,¹ Anna C. Geraghty,¹ Andrea K. Goldstein,¹ Lijun Ni,¹ Pamelyn J. Woo,¹ Ben A. Barres,² Shane Liddelow,^{2,3} Hannes Vogel,⁴ and Michelle Monje^{1,4,5,6,7,8,*}

¹Department of Neurology and Neurological Sciences, Stanford University, Palo Alto, CA 94305, USA

²Department of Neurobiology, Stanford University, Palo Alto, CA 94305, USA

³Department of Neuroscience and Physiology, NYU Neuroscience Institute, New York University School of Medicine, New York, NY 10016, USA

⁴Department of Pathology, Stanford University, Palo Alto, CA 94305, USA

⁵Department of Pediatrics, Stanford University, Palo Alto, CA 94305, USA

⁶Department of Psychiatry and Behavioral Sciences, Stanford University, Palo Alto, CA 94305, USA

⁷Institute for Stem Cell Biology and Regenerative Medicine, Stanford University, Palo Alto, CA 94305, USA

⁸Lead Contact

*Correspondence: mmonje@stanford.edu

<https://doi.org/10.1016/j.cell.2018.10.049>

SUMMARY

Chemotherapy results in a frequent yet poorly understood syndrome of long-term neurological deficits. Neural precursor cell dysfunction and white matter dysfunction are thought to contribute to this debilitating syndrome. Here, we demonstrate persistent depletion of oligodendrocyte lineage cells in humans who received chemotherapy. Developing a mouse model of methotrexate chemotherapy-induced neurological dysfunction, we find a similar depletion of white matter OPCs, increased but incomplete OPC differentiation, and a persistent deficit in myelination. OPCs from chemotherapy-naïve mice similarly exhibit increased differentiation when transplanted into the microenvironment of previously methotrexate-exposed brains, indicating an underlying microenvironmental perturbation. Methotrexate results in persistent activation of microglia and subsequent astrocyte activation that is dependent on inflammatory microglia. Microglial depletion normalizes oligodendroglial lineage dynamics, myelin microstructure, and cognitive behavior after methotrexate chemotherapy. These findings indicate that methotrexate chemotherapy exposure is associated with persistent tri-glial dysregulation and identify inflammatory microglia as a therapeutic target to abrogate chemotherapy-related cognitive impairment.

INTRODUCTION

Chemotherapy causes a syndrome of neurological dysfunction characterized by impaired attention, speed of information pro-

cessing, multitasking, and fine motor and executive function (Bisen-Hersh et al., 2013; Gibson and Monje, 2012; Green et al., 2013). The consequences of this syndrome, also called chemotherapy-related cognitive impairment (CRCI) or colloquially known as “chemobrain,” can be debilitating (Ellenberg et al., 2009). This post-chemotherapy neurological syndrome is well described across numerous populations treated for various adult and pediatric cancers and is particularly prominent when chemotherapeutic regimens include anti-metabolite agents, such as methotrexate (MTX) (Aukema et al., 2009; Gibson and Monje, 2012; Pierson et al., 2016). Although the incidence, severity, and duration of CRCI varies across patient populations and chemotherapeutic regimens, CRCI affects the majority of people treated for cancer, with some studies reporting long-term cognitive dysfunction in over three quarters of patients (reviewed in Wefel and Schagen [2012]). Currently, 15.5 million cancer survivors live in the United States alone, and this number is projected to increase to 20.3 million by 2026 (American Cancer Society, 2016). Thus, CRCI represents a major source of morbidity during and after cancer therapy and a great unmet need to be addressed (Horowitz et al., 2018).

The lasting neurological impact of cancer therapy on survivors, especially of childhood cancer, is not surprising in light of the protracted period of human postnatal neurodevelopment and ongoing cellular neuroplasticity. Myelination, the generation of oligodendrocytes by proliferating oligodendrocyte precursor cells (OPCs) and the formation of the insulating myelin sheath by oligodendrocytes, extends over more than three decades of life (Benes, 1989; Lebel et al., 2012; Yakovlev, 1967) and continues well into adulthood as a form of neuroplasticity (Gibson et al., 2014; McKenzie et al., 2014; Mitew et al., 2018). The constellation of symptoms associated with chemotherapy exposure largely localize to white matter, which is chiefly comprised of myelinated axons. Agents that can, in severe cases, cause clinically evident white matter injury, such as



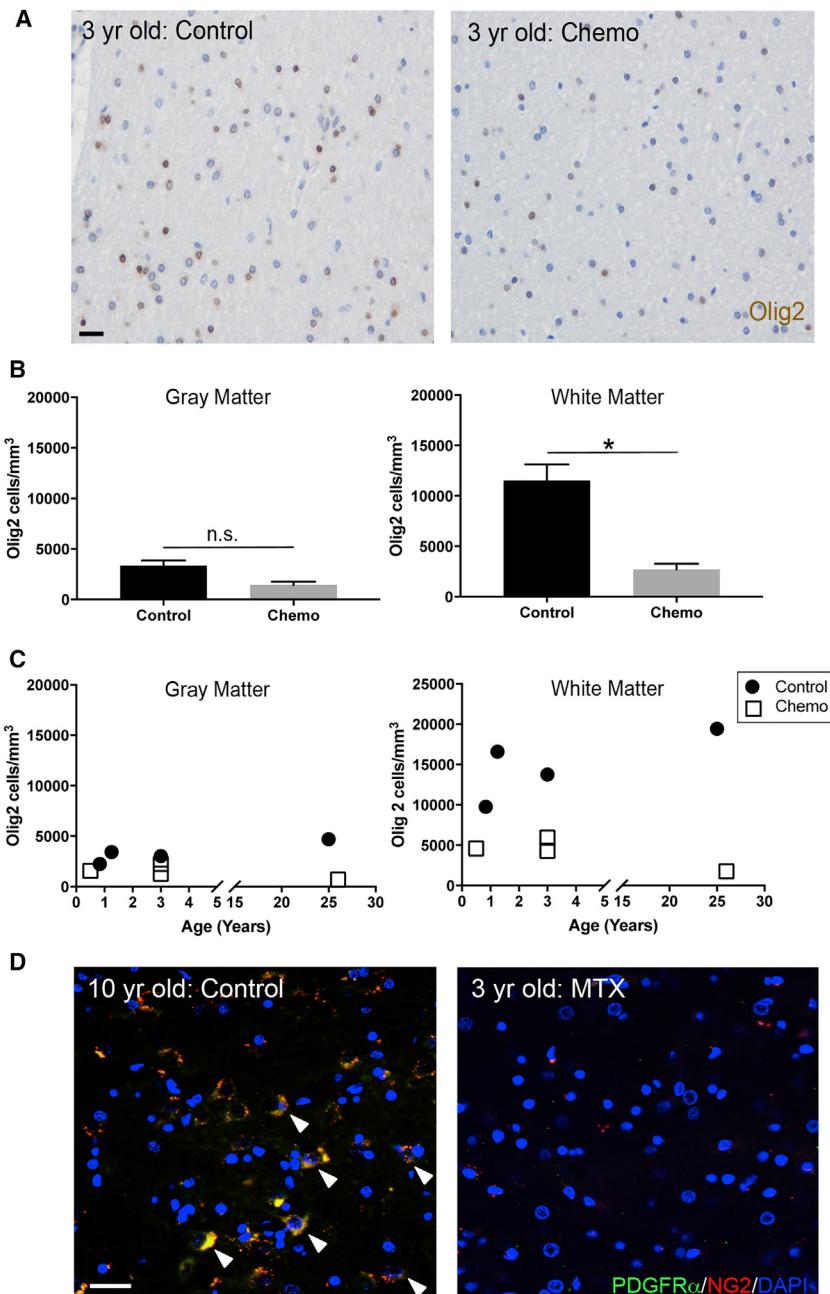


Figure 1. Frontal Lobe White Matter Depletion of Oligodendrocyte Lineage Cells following Chemotherapy

(A) Representative photomicrographs of Olig2⁺ (brown) cells in frontal lobe white matter of a 3-year-old child exposed to chemotherapy and a non-chemotherapy exposed, age-matched control subject.

(B) Chemotherapy exposure selectively depletes Olig2⁺ cells in frontal lobe white matter ($p = 0.0211$; $n = 4$), but not in gray matter ($p = 0.0913$; $n = 4$).

(C) Frontal lobe Olig2⁺ cells throughout early life and young adulthood following chemotherapy treatment, compared to age-matched controls.

(D) Confocal photomicrographs of PDGFR α ⁺/NG2⁺ cells in the frontal lobe subcortical white matter of a 10-year-old male who received no chemotherapy (left) and a 3-year-old male treated with high-dose methotrexate (MTX) chemotherapy (right).

Data shown as mean \pm SEM. n.s. = $p > 0.05$; * $p < 0.05$ by paired t test; $n = 4$ /group. Scale bars, 20 μ m.

See also Table S1.

(Hughes et al., 2013). The long-term effects of chemotherapy on oligodendroglial lineage cell dynamics and myelination remain poorly understood. We hypothesized that long-term OPC population dysregulation or depletion could underlie chemotherapy-associated white matter dysfunction and the associated neurological sequelae of chemotherapy exposure.

RESULTS

Altered Oligodendrocyte Lineage Cell Dynamics in Children and in Young Adults Exposed to Chemotherapy

To determine whether chemotherapy treatment alters human oligodendrocyte lineage cell populations, we examined post-mortem frontal lobe tissue of children and young adults treated with multi-agent chemotherapy in comparison to age-matched control subjects with no history of chemotherapy exposure (Figure 1A; Table S1).

We found that human oligodendrocyte lineage cells, identified by Olig2 expression,

are depleted in subjects with a history of chemotherapy exposure (control: $14,893 \pm 2,063$ cells/mm³ vs. chemo: $4,150 \pm 876$ cells/mm³). This decrease in Olig2⁺ cell density is largely accounted for by deficits in subcortical white matter Olig2⁺ cells (Figure 1B). In contrast, gray matter Olig2⁺ cells are relatively preserved (Figure 1B). In the frontal subcortical white matter of subjects with chemotherapy exposure, Olig2⁺ oligodendroglial lineage cell density is markedly lower compared to age-matched control subjects with no chemotherapy exposure (Figures 1B and 1C). The aforementioned human samples represent archival formalin-fixed, paraffin-embedded human brain specimens

MTX, are particularly associated with long-term neurological deficits (Anderson et al., 2000; Han et al., 2008; Moore et al., 1992; Morioka et al., 2013; Pierson et al., 2016; Winocur et al., 2006).

The mechanisms mediating CRCI have been incompletely understood. Proliferative neural precursor cell populations are sensitive to chemotherapeutic agents (Dietrich et al., 2006; Hyrien et al., 2010; Morris et al., 1995). One robustly cycling population, OPCs (Dawson et al., 2003; Geha et al., 2010), is particularly sensitive to chemotherapeutic agents (Dietrich et al., 2006; Han et al., 2008). However, OPCs rapidly reconstitute to maintain strictly regulated homeostatic population levels in the healthy brain

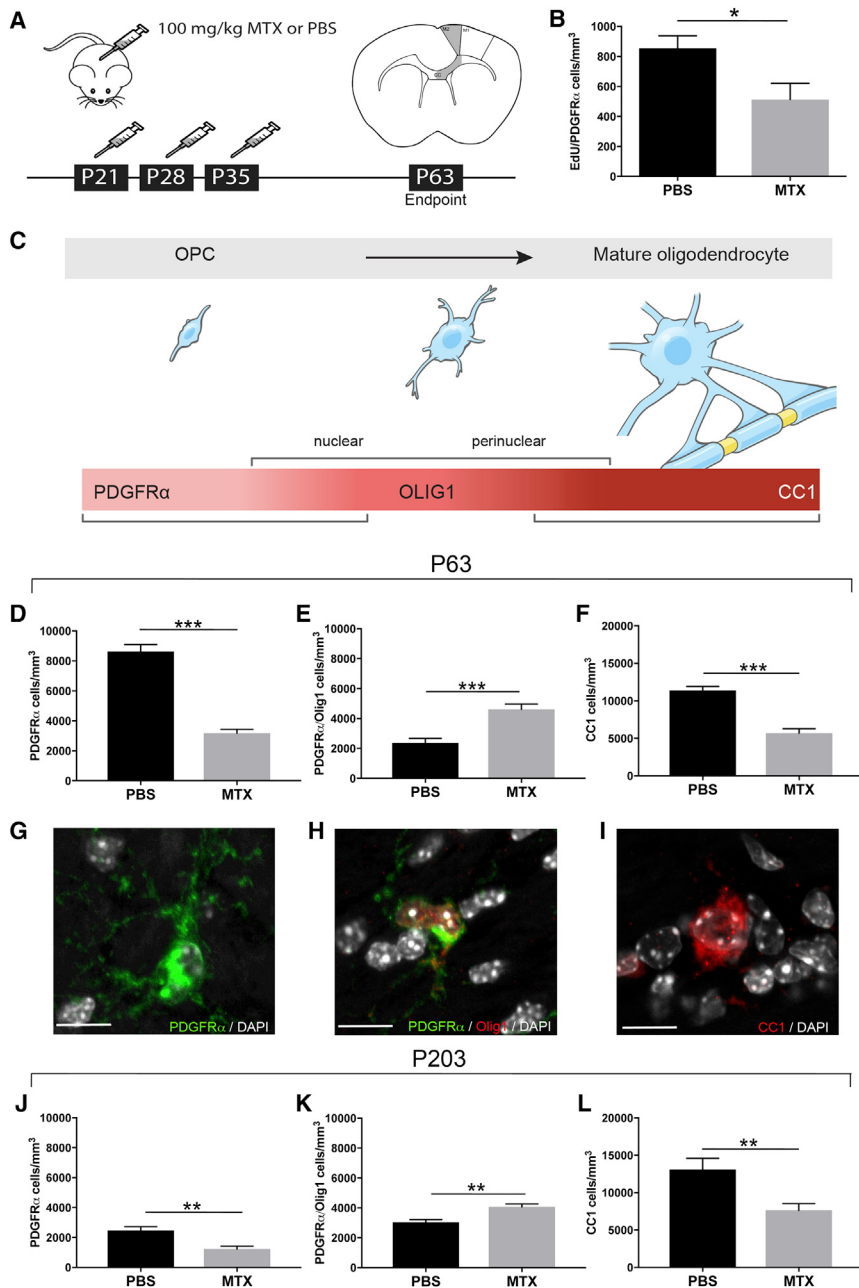


Figure 2. MTX Chemotherapy Exposure Disrupts Oligodendrocyte Lineage Cell Dynamics

(A) Schematic illustration of juvenile MTX exposure paradigm and area of the premotor (M2) circuit analyzed (shaded in gray).

(B) Total cell density of newly proliferated EdU⁺/PDGFR α ⁺ cells at P63 in the corpus callosum of mice exposed to PBS vehicle or MTX on P21, 28, and 35 and injected with 40 mg/kg of EdU on P61, 62, and 63 ($p = 0.0465$; $n = 4$ mice/group).

(C) Schematic illustration of oligodendrocyte lineage cells. OPCs express PDGFR α and begin to express the transcription factor Olig1 in a nuclear and then perinuclear pattern as they progress through differentiation. As differentiation completes, mature, myelinating oligodendrocytes express the marker CC1.

(D–F) Effect of MTX exposure on OPCs (D; PDGFR α ⁺ cells, $p < 0.0001$), PDGFR α ⁺/Olig1⁺ late OPCs (E; $p = 0.0003$), and CC1⁺ mature oligodendrocytes (F; $p < 0.0001$) in the corpus callosum at P63 ($n = 8$ PBS vehicle control mice BS and $n = 7$ MTX mice).

(G–I) Representative confocal photomicrographs of PDGFR α ⁺ OPC (G), PDGFR α ⁺/Olig1⁺ cells (H), and CC1⁺ mature oligodendrocyte (I).

(J–L) Mice ($n = 6$ PBS; $n = 7$ MTX) exposed to juvenile chemotherapy were allowed to age 6 months (P203) post-treatment. MTX-exposed mice exhibit a decrease in white matter OPC cell density (J; $p = 0.002$) and CC1⁺ oligodendrocytes (L; $p = 0.008$) with an increase in late OPCs (K; $p = 0.0003$).

Data shown as mean \pm SEM. * $p < 0.05$; ** $p < 0.01$; *** $p < 0.001$ by unpaired two-tailed Student's t test. Scale bar, 10 μ m.

See also Figures S1 and S2.

Methotrexate Exposure Disrupts Oligodendroglial Lineage Cell Dynamics

To further elucidate the effect of chemotherapy exposure on myelin-forming cells, we developed a mouse model of juvenile high-dose MTX exposure to mimic the histological and functional deficits observed in children after chemotherapy (Figure 2A) (Aukema et al., 2009; Gibson and Monje, 2012). MTX was administered intraperitoneally (i.p.) at 100 mg/kg weekly

for 3 consecutive weeks to mice (starting at P21; Figure 2A). To validate that 100 mg/kg MTX recapitulates the concentrations observed in clinical regimens (Bratlid and Moe, 1978), we used liquid chromatography-tandem mass spectrometry (LC-MS/MS) to assess the concentration of MTX in serum, brain, kidney, and liver 30 min following a single 100 mg/kg injection. We found serum concentrations of MTX in our mouse model ($118 \pm 13 \mu$ M) within the range of those measured in children following high-dose MTX administration (80 – 400μ M; Figure S1A). MTX can directly affect cell viability, so we assessed the IC₅₀ of MTX for a variety of cell types. The MTX IC₅₀ of mouse PDGFR α ⁺ OPCs

for 3 consecutive weeks to mice (starting at P21; Figure 2A). To validate that 100 mg/kg MTX recapitulates the concentrations observed in clinical regimens (Bratlid and Moe, 1978), we used liquid chromatography-tandem mass spectrometry (LC-MS/MS) to assess the concentration of MTX in serum, brain, kidney, and liver 30 min following a single 100 mg/kg injection. We found serum concentrations of MTX in our mouse model ($118 \pm 13 \mu$ M) within the range of those measured in children following high-dose MTX administration (80 – 400μ M; Figure S1A). MTX can directly affect cell viability, so we assessed the IC₅₀ of MTX for a variety of cell types. The MTX IC₅₀ of mouse PDGFR α ⁺ OPCs

(Figures S1B and S1C; 0.14 μ M at 24-hr) and mouse neural precursor cells (Figure S1F) is within the concentration range achieved in the brain (Figure S1A; 0.68 μ M) using our dosage paradigm. By comparison, the MTX IC₅₀ of pediatric brain tumor cultures that do not respond to MTX treatment (Figures S1D and S1E) are unaffected by clinically relevant MTX concentrations. Given the demonstrated concentration of MTX achieved in brain and the OPC IC₅₀, the number of surviving OPCs would be expected to rapidly repopulate the brain to normal numbers in the absence of other pathophysiology (Hughes et al., 2013).

To ascertain whether chemotherapy treatment affected OPC proliferation *in vivo*, we treated mice with MTX or PBS starting at P21 (Figure 2A) and then administered the thymidine analog EdU daily from P61–63 to mark newly proliferating cell populations 1 month after the termination of treatment. The number of newly proliferated EdU⁺/PDGFR α ⁺ OPCs was decreased in the corpus callosum of MTX-exposed mice compared to PBS controls (Figure 2B), although the percentage of OPCs proliferating at this time did not differ (PBS: 12.1% \pm 1.4% vs. MTX: 11.34% \pm 2.95%; $p = 0.85$). Similar to the decreased oligodendroglial cell density found in the human frontal lobe, mice exhibit deficits in the total density of frontal OPCs (PDGFR α ⁺/Olig1⁻ cells). This decrease is predominately driven by deficits in white matter (corpus callosum; 8,618 \pm 469 cells/mm³ vs. 3,181 \pm 259 cells/mm³ in control or MTX-treated mice, respectively; Figures 2C, 2D, 2G, and S2A) and deep cortical gray matter OPCs (Figure S2B) with preservation of superficial cortical gray matter OPCs in the premotor cortex (Figure S2C). Concomitant with the observed decrease in white matter OPCs, MTX-exposed mice exhibited an increase in PDGFR α ⁺/Olig1⁺ cells of intermediate differentiation that we will henceforth call “late OPCs” (Figures 2C, 2E, and 2H). Here we have used Olig1 expression to distinguish earlier OPCs from more differentiated OPCs that co-express Olig1 in a nuclear pattern; if all PDGFR α ⁺ cells irrespective of differentiation state are considered together, a substantial reduction in total OPC density remains evident (PBS: 10,986 \pm 619 cells/mm³ vs. MTX: 7,798 \pm 338 cells/mm³, $p < 0.0008$). The observed increased OPC differentiation appears incomplete as the density of CC1⁺ and perinuclear Olig1⁺ mature oligodendrocytes in the corpus callosum is significantly decreased following MTX chemotherapy treatment (Figures 2C, 2F, 2I, and S2D). While we observed a significant increase in apoptotic cells, as identified by cleaved caspase-3 24hr following a single MTX injection, levels of apoptosis were drastically reduced 4 weeks following MTX and none of the identified apoptotic cells co-expressed PDGFR α at the 4-week time point (Figures S2E and S2F). Thus, in contrast to the expected homeostatic behavior of healthy OPCs (Hughes et al., 2013), the white matter OPC population does not repopulate to normal levels following MTX chemotherapy exposure due in part to decreased OPC proliferation and increased OPC differentiation, but not attributable to ongoing OPC apoptosis.

Because many cancer patients report cognitive deficits following chemotherapy that can persist for years after the termination of treatment (Aukema et al., 2009; Pierson et al., 2016), we followed a cohort of mice that were treated with MTX or PBS vehicle for 6 months following the end of treatment (P203). Similar to the 4-week time point (P63), at P203 mice exposed

to juvenile MTX exhibit decreases in PDGFR α ⁺ OPCs (Figure 2J) and CC1⁺ mature oligodendrocytes (Figure 2L) with concomitant increases in PDGFR α ⁺/Olig1⁺ late OPCs (Figure 2K) compared to controls. Thus, oligodendroglial lineage dynamics are consistently perturbed for at least 6 months following MTX chemotherapy.

Juvenile Chemotherapy Exposure Disrupts Myelination and Behavioral Function

Standard neuroimaging of patients who are experiencing chemotherapy-related neurological impairments typically exhibit no evidence of overt demyelination. Concordantly, we found that gross myelin appearance in the corpus callosum following MTX exposure remained intact as assessed by the presence and distribution of myelin basic protein (MBP; Figures 3A, 3B, S3A, and S3B). Corpus callosum volume was unchanged between PBS- and MTX-treated mice, indicating that the observed changes in OPC density were not a result of altered volume of the corpus callosum (Figure 3C). However, using transmission electron microscopy (TEM) to evaluate myelin microstructure, we observed a substantial decrease in myelin sheath thickness as indicated by an increased *g*-ratio of projections to corpus callosum at the level of the cingulum in MTX-exposed mice at 4 weeks following treatment compared to vehicle controls (*g*-ratio = diameter of axon/diameter of entire fiber; PBS: 0.746 \pm 0.0049; MTX: 0.801 \pm 0.00785; Figures 3D–3G and S3C). Axons of all caliber exhibited decreased myelin thickness in mice at both 4 weeks (Figure 3G) and 6 months (Figures 3H, 3I, and S3G) following MTX exposure. These data indicate that MTX chemotherapy is associated with lasting changes to myelin microstructure.

The dysregulation of OPC lineage dynamics and myelination in this mouse model are accompanied by behavioral deficits characteristic of chemotherapy sequelae, including decrements in motor function (Green et al., 2013). Forepaw swing speed, a measure of limb movement speed sensitive to alterations in the motor system broadly, is modulated by changes in myelin microstructure in the premotor circuit (Gibson et al., 2014). Forepaw swing speed was decreased in MTX-exposed mice 4 weeks following chemotherapy treatment (101.6 \pm 4.6 cm/s vs. 74.4 \pm 7.8 cm/s; Figure S3D). Other parameters of gait, such as stride length, were not altered (Figure S3E). Anxiety, a neuropsychiatric symptom associated with chemotherapy exposure (Bray et al., 2017), was also evident in this model. MTX-exposed mice spent less time in the middle of an open field than PBS vehicle-treated controls (Figure S3F). The hallmark neurological symptoms following chemotherapy treatment are cognitive deficits (Bisen-Hersh et al., 2013; Seigers et al., 2009; Winocur et al., 2006; Zhou et al., 2016), especially those associated with attention-based tasks (Pierson et al., 2016). To determine whether cognitive behavior was compromised following juvenile chemotherapy treatment, we assessed attention and short-term memory using a modified novel object recognition task (NORT) 4 weeks after MTX treatment in which we shortened the time between the training and testing phases to skew the test toward attentional function. Both PBS- and MTX-exposed mice explored the objects an equivalent amount of time during the training phase (Figure 3J). During the testing phase, the control animals exhibited a preference toward the novel object, whereas

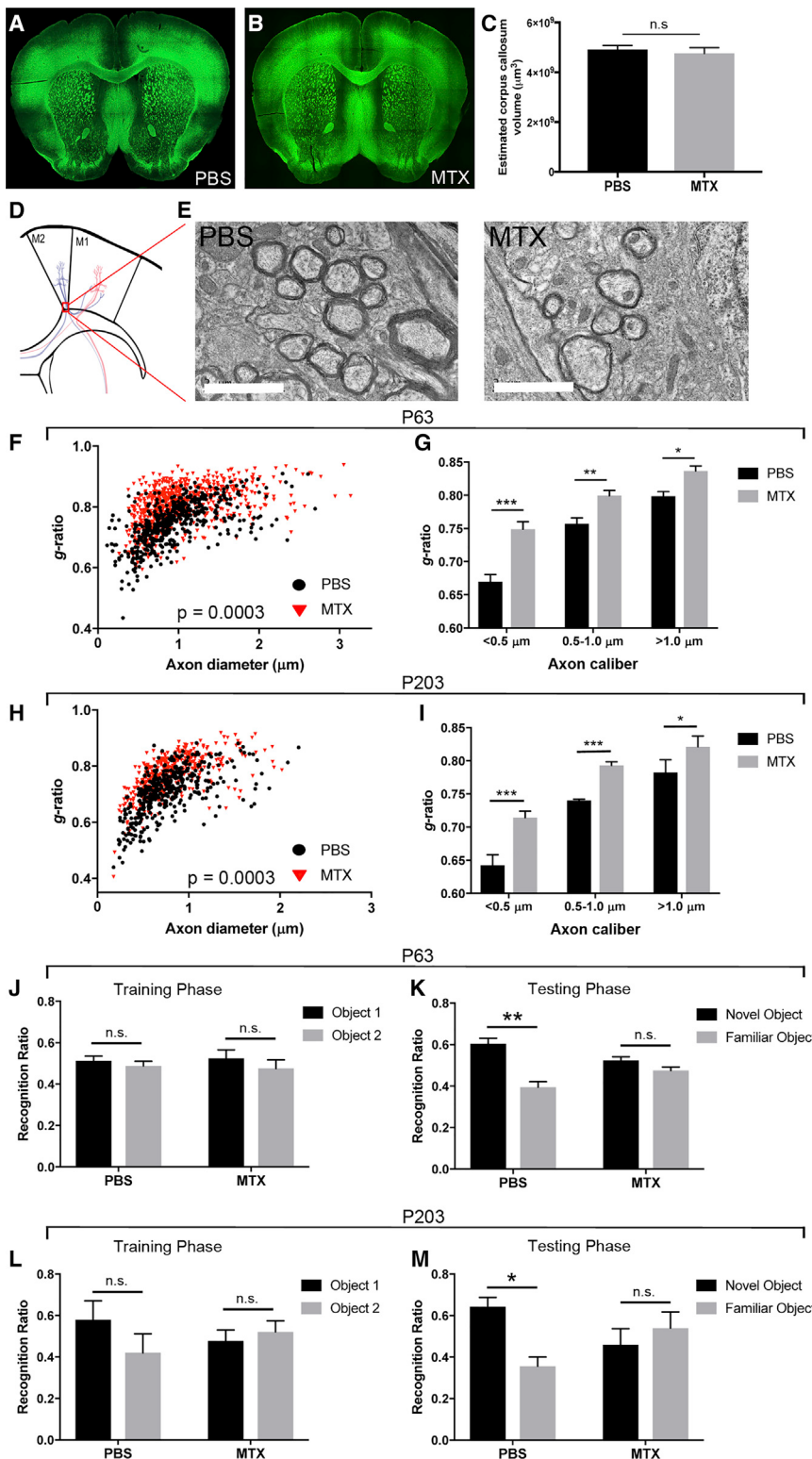


Figure 3. Persistent Myelin and Neurological Deficits following Juvenile Chemotherapy Exposure

(A and B) Confocal photomicrographs of myelin basic protein (MBP) in PBS- (A) and MTX-exposed (B) mouse brains (coronal sections).

(C) Corpus callosum volume of P63 mice exposed to PBS or MTX (p = 0.592; n = 5 PBS vehicle control mice; n = 4 MTX-exposed mice)

(D) Schematic illustration of the premotor cortex and subcortical projections, indicating the region assessed at the level of the cingulum using transmission electron microscopy (TEM; red box).

(E) Representative TEM images of premotor (M2) projections in PBS- and MTX-exposed mice. Scale bar, 2 μm .

(F) Scatterplots of *g*-ratio as a function of axon diameter of M2 projections at P63 (PBS: *g*-ratio 0.7464 ± 0.0049 , n = 5 mice; MTX: *g*-ratio 0.801 ± 0.00785 , n = 8 mice; p = 0.0003).

(G) The increase in *g*-ratio in MTX-exposed mice compared to PBS-exposed mice at P63 occurs in small (< 0.5 μm ; p < 0.0001), medium (0.5–1.0 μm ; p = 0.0097), and large (> 1.0 μm ; p = 0.0220) caliber axons. n = 5 PBS mice; n = 8 MTX mice.

(H) Scatterplots of *g*-ratio as a function of axon diameter of M2 projections at P203 (PBS: *g*-ratio 0.7073 ± 0.0037 , n = 4 mice; MTX: *g*-ratio 0.7697 ± 0.0073 , n = 4 mice; p = 0.0003).

(I) The increase in *g*-ratio in MTX- compared to PBS-exposed mice at P203 occurs in small (< 0.5 μm ; p < 0.0001), medium (0.5–1.0 μm ; p < 0.0001), and large (> 1.0 μm ; p = 0.0188) caliber axons. n = 4 mice PBS; n = 4 mice MTX.

(J) P63 PBS- and MTX-exposed mice spent equivalent amounts of time exploring object 1 and object 2 during the training phase of NORT (PBS: p = 0.59, n = 9 mice; MTX: p = 0.58, n = 7 mice).

(K) During the testing phase of NORT, PBS-exposed mice spent significantly more time exploring the novel object compared to the familiar object (p = 0.004), whereas MTX-exposed mice did not discriminate between the objects (p = 0.18).

(L and M) P203 PBS- and MTX-exposed mice spent equivalent amounts of time exploring object 1 and object 2 during the training phase of NORT (L; PBS: p = 0.45, n = 4; MTX: p = 0.69, n = 7) but during the testing phase (M), PBS-exposed mice spent significantly more time exploring the novel compared to the familiar object (p = 0.047), whereas the MTX-exposed mice did not discriminate between the objects (p = 0.62).

Data shown as mean \pm SEM. *p < 0.05; **p < 0.01; ***p < 0.001; n.s. p > 0.05 by unpaired two-tailed Student's t test.

See also Figure S3.

MTX-treated mice did not discern between the two objects (Figure 3K). At P203, mice exposed to juvenile MTX continued to exhibit deficits in the ability to discriminate between the novel

and familiar objects at 6 months post-treatment, consistent with a persistent cognitive deficit following MTX exposure (Figures 3L and 3M). Collectively, these data demonstrate that this mouse model exhibits behavioral deficits similar to the symptoms humans experience after chemotherapy.

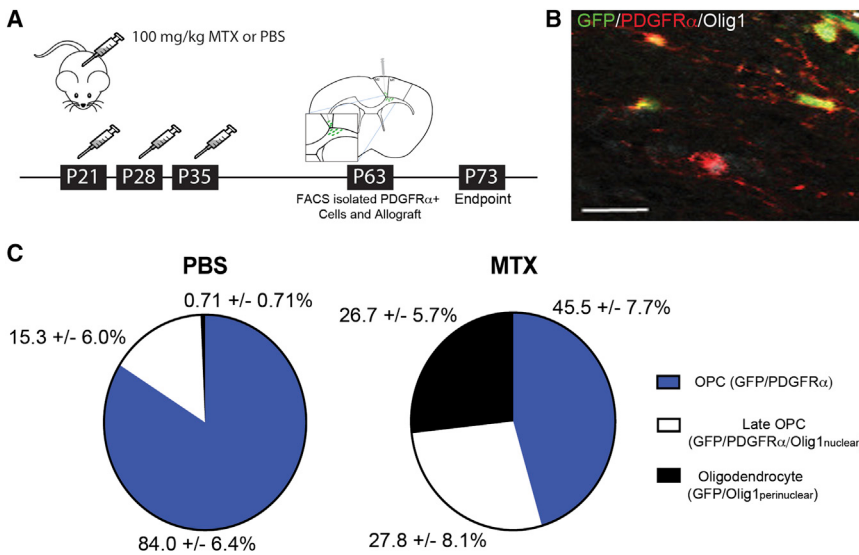


Figure 4. Microenvironmental Perturbation Drives Differentiation of Oligodendrocyte Precursor Cells

(A) Schematic illustration of juvenile chemotherapy paradigm and syngeneic transplantation of GFP⁺/PDGFR α ⁺ cells.

(B) Confocal photomicrograph of transplanted GFP⁺/PDGFR α ⁺ cells in the corpus callosum 10 days post-transplantation (GFP, green; PDGFR α , red; Olig1, white). Scale bar, 20 μ m.

(C) Syngeneic transplantation of GFP⁺/PDGFR α ⁺ cells into previously MTX- ($n = 3$ mice) or PBS-exposed ($n = 4$ mice) corpus callosi. Percentage of cells GFP⁺/PDGFR α ⁺ ($p = 0.01167$), GFP⁺/PDGFR α ⁺/Olig1^{nuclear} ($p = 0.259$), and GFP⁺/Olig1^{perinuclear} oligodendrocytes ($p = 0.00295$) in MTX- and PBS-exposed mice 10 days post-transplantation. Data shown as mean \pm SEM; unpaired two-tailed Student's t test. See also Figure S4.

Perturbations of the Gliogenic Microenvironment Persist Long After Exposure to Methotrexate

Next, we tested the extent to which the changes in oligodendroglial lineage dynamics reflect microenvironmental alterations after MTX. Chemotherapy-naive PDGFR α ⁺ cells isolated by fluorescence-activated cell sorting (FACS) from GFP⁺ transgenic mice were transplanted into the cingulum of the corpus callosum of P63 mice previously treated with MTX or PBS vehicle (Figures 4A and 4B). The sorted population of GFP⁺/PDGFR α ⁺ cells obtained had a purity of 98%, with little contamination by other cell types, including Iba1⁺ microglia (Figure S4). Analysis of the transplanted GFP⁺ cells at 10 days following transplantation revealed that 84% \pm 6.4% remained PDGFR α ⁺ OPCs in PBS-exposed mice, while only 45.5% \pm 7.7% remained OPCs in the brains of mice previously exposed to MTX (%GFP⁺/PDGFR α ⁺; $p = 0.0117$). An equivalent proportion of GFP⁺ cells represented late OPCs (%GFP⁺/PDGFR α ⁺/Olig1^{nuclear}) at this time point in both PBS- and MTX-exposed brains, with significantly more GFP⁺ cells differentiating into perinuclear Olig1⁺ oligodendrocytes in mice exposed to MTX (%GFP⁺/Olig1^{perinuclear}; Figure 4C). These data reveal that MTX chemotherapy exerts sustained changes to the gliogenic microenvironment that foster OPC differentiation. While increased OPC differentiation of the transplanted cells at this time point can be attributed to microenvironmental changes induced by MTX, the transplanted OPCs did not exhibit a blockade in full oligodendrocyte maturation. One interpretation is that the deficit in full oligodendrocyte maturation exhibited by endogenous OPCs reflects changes induced by either exposure to the MTX-altered microenvironment from the time of initial drug treatment and/or previous direct MTX toxicity.

Chemotherapy-Induced Activation of White Matter Microglia

Previous work has shown that disruptions in the microenvironment, including neuroinflammatory microglia, can alter precursor

cell populations (Briones and Woods, 2014; Monje et al., 2002, 2003; Seigers et al., 2009). To investigate this possibility following chemotherapy exposure, we analyzed microglial populations in our juvenile MTX exposure model. We found that activated CD68⁺/Iba1⁺ microglia are increased in the white matter (PBS: 3,242 \pm 474 cells/mm³ vs. MTX: 6,504 \pm 529 cells/mm³), but not the gray matter of the premotor circuit at P63 in MTX-treated mice compared to vehicle controls (Figures 5A, 5B, and 5D). This chemotherapy-induced increase in white matter microglial activation persisted at least 6 months after MTX (Figure 5C). To confirm the activation state of microglia 4 weeks after the cessation of chemotherapy treatment, we sorted Iba1⁺ microglia by FACS from frontal deep cortex and corpus callosum of P63 mice that were previously exposed to PBS or MTX. MTX-exposed microglia expressed increased levels of activation gene transcripts, as determined by microfluidic qPCR (Figure 5E). We then isolated microglia from P5 animals and exposed them *in vitro* to 0.68 μ M of MTX for 24 hr to determine whether MTX directly regulated microglial activation. MTX-treated microglia exhibited increased activation compared to PBS control-treated microglia (Figure 5F), indicating a direct mechanism of neuroinflammatory microglial activation by MTX.

Activated Microglia Induce Reactivity in Astrocytes following Methotrexate Exposure

Recent work has shown that activated microglia can induce reactivity in astrocytes and may be associated with long-term deficits in some neurological diseases (Liddelow et al., 2017). To determine whether the persistent MTX-induced microglial activation resulted in astrocyte reactivity, we first exposed astrocytes *in vitro* to physiologically relevant concentrations of MTX for 24 hr (Figure S1A). MTX, even at high concentrations (1.36 μ M), did not directly induce reactivity of astrocytes *in vitro* (Figure 6A). However, when we induced reactivity in microglia *in vitro* through MTX exposure and placed the

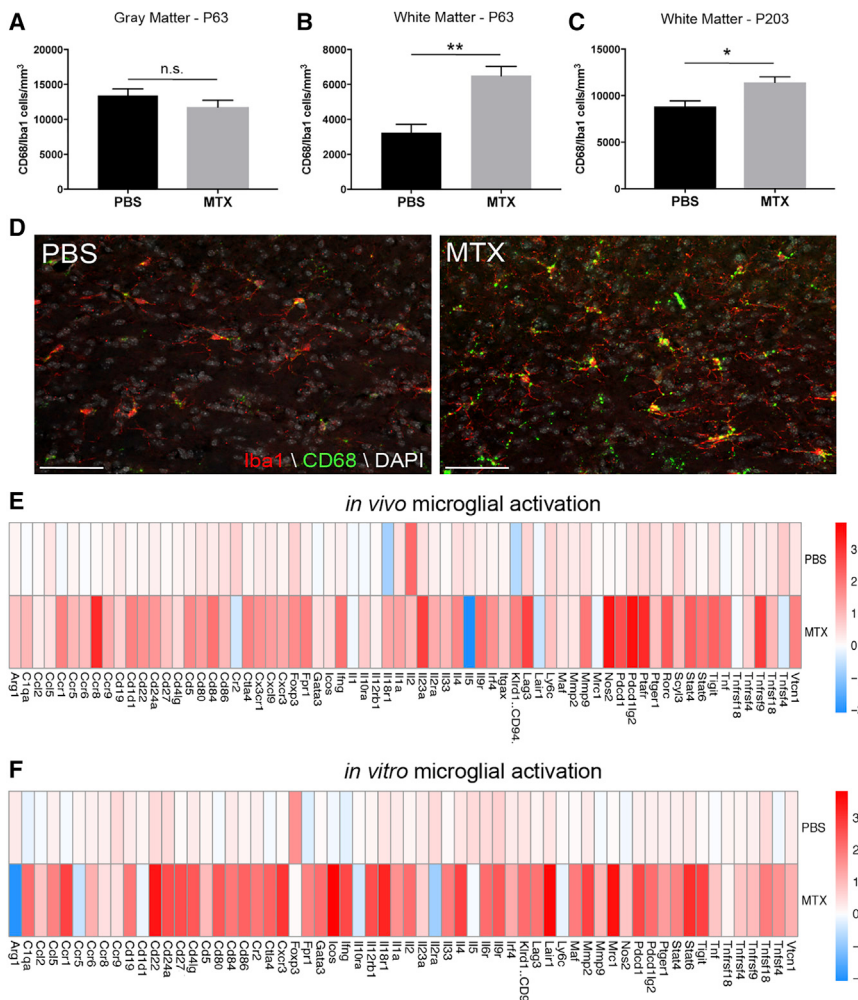


Figure 5. Chronic Microglial Activation Is Secondary to MTX Exposure

(A–C) Activation of microglia ($CD68^+/Iba1^+$) following chemotherapy exposure in the superficial cortical gray matter (A; $p = 0.2570$) and corpus callosum (B; $p = 0.0018$) at P63 ($n = 5$ mice/group) and P203 (C; $p = 0.01$; $n = 7$ mice/group). Data shown as mean \pm SEM. * $p < 0.05$; ** $p < 0.01$; n.s. $p > 0.05$ by unpaired two-tailed Student's t test.

(D) Confocal photomicrographs of $CD68^+/Iba1^+$ activated microglia in the corpus callosum at P63 ($Iba1$, red; $CD68$, green; DAPI, white). Scale bar, 50 μ m.

(E) Iba^+ microglia were isolated using FACS at P63 from frontal deep cortex and corpus callosum of previously PBS- or MTX-exposed mice ($n = 2$ –6 mice/condition/sort). Heatmap of activated transcripts indicate a significant increase in activation following MTX exposure ($p < 0.0001$).

(F) Immunopanned microglia exposed to 0.68 μ M of MTX for 24 hr *in vitro* indicate significant activation compared to vehicle control ($p < 0.0001$). All experiments analyzed by two-way ANOVA with Tukey post hoc tests and performed with $n = 3$ biological replicates (E and F).

See also Table S2.

conditioned medium from these MTX-induced activated microglia (MTX-MCM) on astrocytes for 24 hr, we initiated broad reactivity of astrocytes compared to PBS vehicle-treated medium. This astrocyte reactive phenotype was not constrained to a single subtype of reactive response (A1 or A2; Zamanian et al., 2012) (Figure 6A). Next, we investigated the reactive state of astrocytes from our mouse model. *ALDH1L1::eGFP* astrocyte reporter mice (Yang et al., 2011) were treated with MTX or PBS as above. At P63, we sorted astrocytes from frontal deep cortex and corpus callosum by FACS. Astrocytes exposed to MTX *in vivo* exhibited increased reactivity as indicated by an upregulation of pan-reactive (upregulated in both A1 and A2 astrocytes) and A2-specific but not A1-specific genes (Figure 6B).

Microglial Depletion Reverses the Deleterious Effects of Chemotherapy-Induced Glial Dysregulation

Next, we aimed to determine whether activated microglia are necessary for MTX chemotherapy-induced alterations to oligodendrocyte lineage cell dynamics and function. Mice underwent the same juvenile chemotherapy treatment paradigm

described above, and at P38 half of the MTX- and PBS-exposed mice received chow containing PLX5622, a small-molecule compound that inhibits colony-stimulating factor 1 receptor (CSF1R), required for microglial survival. The other half received control chow (Figure 7A). PLX5622 administration has been shown to significantly deplete microglia within 7 days (Dagher et al., 2015; Elmore et al., 2014). As expected, the MTX-

exposed mice exhibited an increase in $Iba1^+$ microglia compared to PBS-treated controls (Figure 7C) when fed control chow. Both MTX- and PBS-exposed cohorts that received PLX5622 chow for the 26 days following treatment exhibited a 70%–80% reduction in $Iba1^+$ microglia in the corpus callosum compared to animals fed control chow (Figures 7B and 7C).

To determine whether astrocyte reactivity due to MTX-induced microglial activation is normalized with microglial depletion, pan-astrocyte reactivity in PBS- and MTX-exposed mice with and without PLX5622 treatment was assessed using RNAscope for the pan-reactive marker *Cxcl10* and the astrocytic marker *Glast*. Following MTX exposure, we found a significant increase in the percentage of *Glast* $^+$ astrocytes with high numbers of *Cxcl10* puncta (>8 puncta/cell) in MTX-exposed compared to PBS-exposed mice ($27.2\% \pm 6.5\%$ vs. $1.49\% \pm 0.24\%$; Figures 7D and S5A). The percentage of reactive astrocytes is substantially reduced when microglia are depleted following MTX exposure ($9.17\% \pm 2.7\%$; Figures 7D and S5A), indicating that microglial depletion can reduce astrocyte reactivity following chemotherapy.

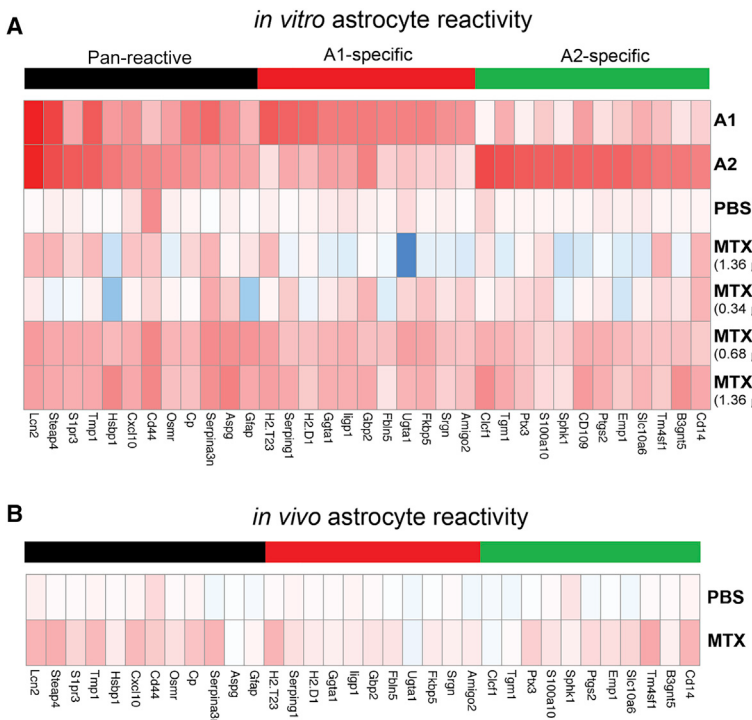


Figure 6. Chemotherapy-Exposed Activated Microglia Induce Astrocyte Reactivity

(A and B) Heatmaps depicting mRNA expression levels of astrocyte reactivity gene transcripts.

(A) Immunopanned astrocytes directly exposed to high ($1.36 \mu\text{M}$) concentrations of MTX *in vitro* do not become reactive, but when exposed to conditioned medium from MTX-induced activated microglia ($0.68 \mu\text{M}$ MTX-MCM) astrocytes become broadly reactive compared to PBS vehicle-exposed controls (Pan-reactive genes (black bar), $p = 0.0004$; A1-specific genes (red bar), $p = 0.0193$; A2-specific genes (green bar), $p = 0.0144$).

(B) Astrocytes were isolated using FACS from *ALDH1L1::eGFP* mice at P63 that were previously exposed to PBS or MTX in the juvenile period. MTX exposure results in broad astrocyte reactivity compared to PBS exposure ($n = 4-5$ mice/condition/sort; pan-reactive, $p = 0.0011$; A1, $p = 0.075$; A2, $p = 0.0097$).

All experiments analyzed by two-way ANOVA with Tukey post hoc tests and performed with $n = 3$ biological replicates.

See also Table S2.

Similarly, treatment with PLX5622 normalized the MTX-induced decrease in PDGFR α^+ OPC density (PBS-control $10,221 \pm 1,446$ cells/mm 3 vs. MTX-PLX5622 $11,113 \pm 351$ cells/mm 3 , $p = 0.9996$) and increase in PDGFR $\alpha^+/\text{Olig}1^+$ late OPCs (PBS-control $2,083 \pm 367$ cells/mm 3 vs. MTX-PLX5622 $2,930 \pm 746$ cells/mm 3 , $p = 0.5437$) to levels seen in PBS control animals (Figure 7E). Microglial depletion also partially restored CC1 $^+$ oligodendrocyte density compared to MTX-control levels (Figure 7E). Taken together, these data reveal that MTX chemotherapy-induced microglial activation is necessary for persistent alterations to oligodendrocyte lineage cell populations following chemotherapy exposure.

To determine whether depletion of microglia can rescue chemotherapy-induced myelin deficits, PBS- or MTX-exposed animals were fed control or PLX5622 chow from P38–63 and sacrificed for analysis using TEM at P63. Microglial depletion following chemotherapy treatment normalized overall myelin sheath thickness in MTX-exposed/PLX5622-treated mice to control levels (Figures 7F–7I). The normalization of myelin sheath thickness to PBS-control levels occurred in small, medium, and large caliber axons (Figure S5B). The average axon diameter did not differ between groups (Figure S5C).

To evaluate possible functional consequences of microglial depletion in MTX-exposed mice, we assessed cognitive behavior at P63 using the modified NORT described above (Figures 7J–7K). As above, MTX-exposed mice fed control chow, allowing for persistent microglial activation, exhibited an inability to discriminate between the novel and familiar objects during the testing phase (Figure 7K). In contrast, microglial depletion with PLX5622 in MTX-exposed mice rescued this chemotherapy-induced behavioral deficit (Figure 7K). Taken together,

these data indicate that microglial activation is necessary for the persistent dysregulation of oligodendrocyte lineage cells, myelin, and astrocytes as well as the behavioral deficits observed following MTX chemotherapy exposure.

DISCUSSION

Dysregulation of the OPC Population in White Matter Diseases

While previous work has demonstrated broad neural precursor cell population sensitivity to chemotherapy exposure (Dietrich et al., 2006; Han et al., 2008; Hyrien et al., 2010; Morris et al., 1995), this lasting depletion of the OPC population after MTX chemotherapy was unexpected; OPCs typically maintain a precise homeostatic density and can rapidly repopulate after injury (Baxi et al., 2017; Hughes et al., 2013). The inability of the residual OPC population to replenish to normal levels suggests a long-term dysregulation of OPC homeostasis in the post-chemotherapy microenvironment. Typically, MTX is cleared from CSF by 72 hr after administration (Bratlid and Moe, 1978); however, the possibility that very low levels remain in tissue long-term cannot be completely excluded. While the inability of the OPC population to recover following MTX chemotherapy was surprising, the differential response to chemotherapy between gray and white matter OPCs supports an emerging principle of glial heterogeneity in the healthy and diseased brain (Baxi et al., 2017; Viganò et al., 2013). The functional consequences of the observed accumulation of intermediate oligodendrocyte progenitors following MTX exposure is highlighted by the continued decrement in mature, myelinating oligodendrocytes at both one and 6 months after treatment. This blockade of full differentiation mirrors dysregulation of OPC differentiation in white matter lesions associated with multiple sclerosis (MS; for review, see

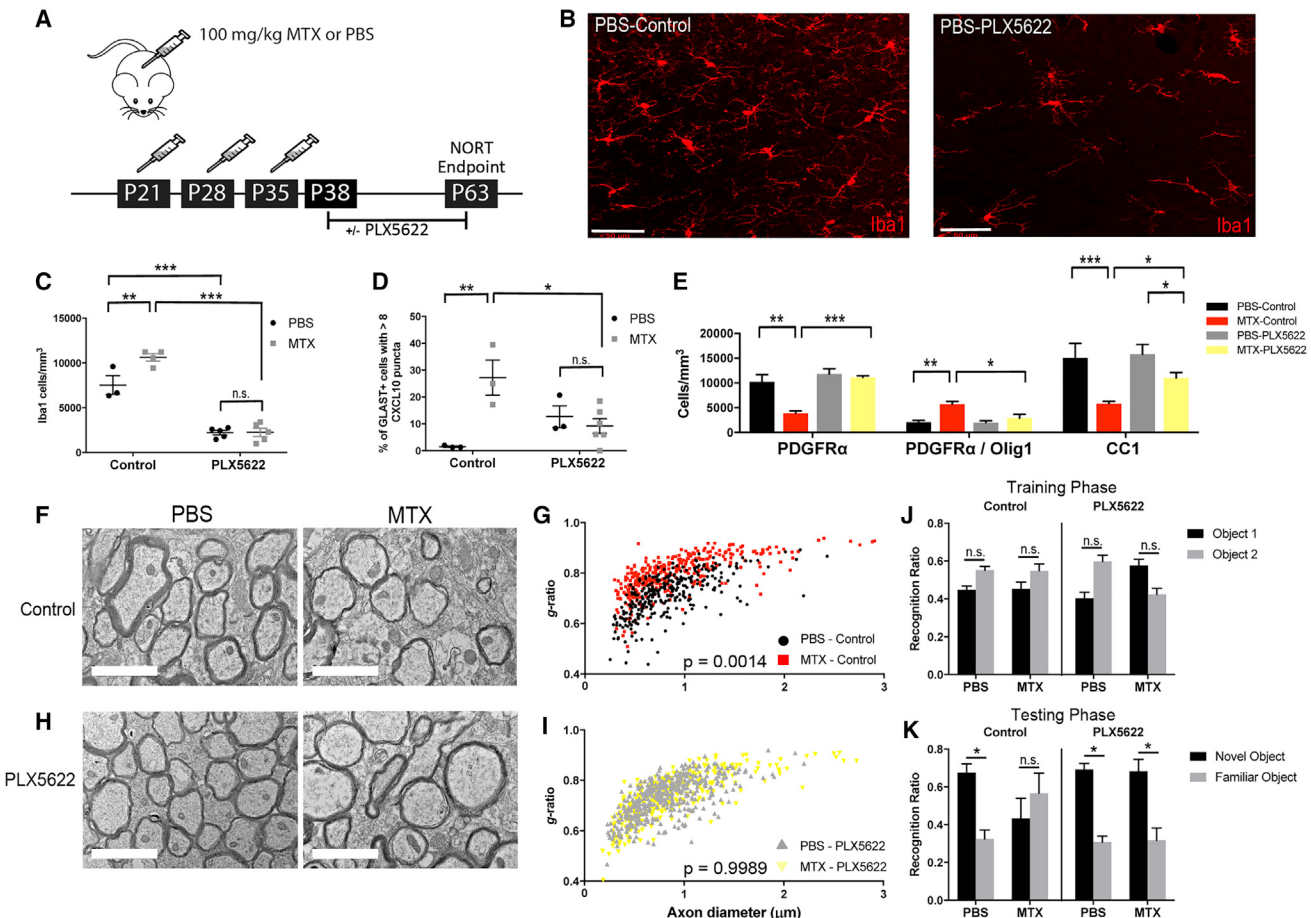


Figure 7. Microglial Depletion Rescues Chemotherapy-Induced Deficits in Oligodendroglial Lineage Cell and Astrocytic Dynamics, Myelination, and Cognitive Behavior

(A) Schematic of juvenile chemotherapy exposure paradigm plus microglial depletion with PLX5622.

(B) Confocal photomicrographs of Iba1⁺ microglia in the corpus callosum of PBS-exposed mice fed control or PLX5622 chow. Scale bar, 50 μ m.

(C) Iba1⁺ microglia are decreased by 70%–80% in PBS and MTX mice following 26 days of PLX5622 (PBS-control n = 3 vs. MTX-control n = 4; p = 0.0092; PBS-control vs. PBS-PLX5622 n = 5 mice/group; p < 0.0001; MTX-control vs. MTX-PLX5622 n = 5; p < 0.0001) by two-way ANOVA with Tukey post hoc analyses.

(D) Microglial depletion normalizes the percentage of Glast⁺ astrocytes with high expression levels, measured by mRNA puncta, of the pan-reactive gene Cxcl10 in MTX- compared to PBS-exposed mice (PBS-control n = 3 vs. MTX-control n = 3, p = 0.0053; MTX-control vs. MTX-PLX5622 n = 6, p = 0.0207; PBS-control vs. PBS-PLX5622 n = 3; p = 0.28).

(E) Microglial depletion increases OPC (p = 0.0002) and mature oligodendrocyte (p = 0.0106) but decreases late OPC (p = 0.0174) cell density in MTX mice fed PLX5622 chow compared to MTX mice fed control chow. The CC1⁺ mature oligodendrocyte population is partially recovered to PBS levels (p = 0.0128) by one-way ANOVA. PBS-control n = 3 mice; MTX-control n = 4 mice; PBS-PLX5622 and MTX-PLX5622 n = 5 mice/group.

(F) Representative TEM images of cortical projections to corpus callosum at the level of the cingulum in PBS and MTX mice treated with control chow. Scale bar, 2 μ m.

(G) Scatterplots of individual axons as a function of axon diameter for PBS and MTX mice fed control chow. g-ratio: PBS-control (n = 3) 0.7151 \pm 0.014; MTX-control (n = 3) 0.7953 \pm 0.015, p = 0.0014.

(H) Representative TEM images of cortical projections to corpus callosum at the level of the cingulum in PBS and MTX mice treated with PLX5622 chow. Scale bar, 2 μ m.

(I) Scatterplots of individual axons as a function of axon diameter for PBS and MTX mice fed PLX5622 chow. PBS-PLX5622 (n = 4) 0.7331 \pm 0.0035; MTX-PLX5622 (n = 3) 0.735 \pm 0.0023, p > 0.05; MTX-control vs. MTX-PLX5622 p = 0.0089.

(J and K) Novel Object Recognition Test (NORT) in PBS- or MTX-exposed mice at P63 following treatment with control or PLX5622 chow.

(J) During the NORT training phase, mice spent equivalent time exploring object 1 and object 2, regardless of juvenile chemotherapy treatment or post-treatment microglial state; PBS-control (n = 5), p = 0.057; MTX-control (n = 3), p = 0.32; PBS-PLX5622 (n = 3), p = 0.10; MTX-PLX5622 (n = 5), p = 0.08.

(K) During the testing phase, PBS-control (p = 0.02), PBS-PLX5622 (p = 0.027), and MTX-PLX5622 (p = 0.047) mice explored the novel object significantly more than the familiar object, whereas MTX-control mice (p = 0.59) did not discriminate between the novel and familiar objects.

Data are shown as the mean \pm SEM. *p < 0.05; **p < 0.01; ***p < 0.001; n.s. p > 0.05. Two-way ANOVA with Tukey post hoc tests (C, D, G, I), one-way ANOVA with Tukey post hoc tests (E), unpaired, two-tailed Student's t test (J, K).

See also Figure S5.

Miron et al., 2011). OPCs transplanted to the brains of previously MTX-exposed mice exhibit a similar increase in OPC differentiation, but unlike resident OPCs these transplanted cells continue through the maturation process. Full maturation of the transplanted, chemotherapy-naïve OPCs suggests that the chemotherapy-induced blockade of full differentiation exhibited by endogenous cells may be due to cell-intrinsic changes following MTX treatment and/or more extensive exposure to the MTX-altered microenvironment from the time of the initial insult. The partial rescue of normal oligodendrocyte numbers and rescue of myelin microstructure following a period of microglial depletion underscores the importance of the microenvironmental perturbations after MTX. The mechanism(s) mediating the inability of OPCs to fully differentiate into mature oligodendrocytes in neuroinflammatory disease states, such as CRCI and MS, remain a pressing question in the field.

Oligodendrocyte Dynamics in Health and in Disease

Adult-born, mature oligodendrocytes exhibit lasting stability throughout much of the lifespan of healthy animals (Hill et al., 2018; Hughes et al., 2018; Tripathi et al., 2017). This protracted survival of mature oligodendrocytes results in a dramatic cellular accumulation throughout adulthood thought to contribute to ongoing changes in myelin microstructure (Tripathi et al., 2017). The production of new oligodendrocytes is required for learning new motor skills during adulthood (McKenzie et al., 2014; Xiao et al., 2016), and plasticity of myelin may contribute more broadly to learning and cognition (for discussion, see Mount and Monje [2017]). The persistent chemotherapy-induced decrement in myelinating oligodendrocytes and associated behavioral deficits further underscores the importance of maintaining proper oligodendroglial dynamics to support healthy neurological functioning.

Neuroinflammatory Microglia Disrupt Precursor Cell Populations

The persistent disruption of the gliogenic microenvironment following MTX exposure is concordant with a developing principle of cancer therapy-induced neural precursor cell dysfunction (Gibson and Monje, 2012). Cranial radiation decreases hippocampal neurogenesis (Monje et al., 2002, 2007; Parent et al., 1999) by inducing chronic microglial inflammation (Monje et al., 2003). MTX chemotherapy exposure has been previously shown to increase microglial inflammation in adult rats (Seigers et al., 2010), which we have demonstrated in this murine model to be largely restricted to the white matter. The regional heterogeneity observed in microglial responses to MTX chemotherapy are consistent with our understanding of regional heterogeneity in microglia throughout the brain (Hagemeyer et al., 2017; Grabert et al., 2016). Long-term microglial inflammation following chemotherapy treatment may vary among agents, as microglial activation has been described following exposure to some chemotherapeutic agents, such as MTX (Seigers et al., 2010) and carboplatin (Acharya et al., 2015), but not with others, such as cisplatin and 5-FU (Han et al., 2008; Zhou et al., 2016). Thus, while the neurotoxic pathophysiology of many commonly used cancer therapies, such as radiation and MTX, include a central role for activated microglia, it is important to note that

diverse cancer therapies will involve a range of pathophysiological mechanisms.

Microglial depletion strategies to address cancer therapy-associated cognitive impairment will need to be carefully studied in a tumor-specific fashion. Ideal timing of microglial depletion, whether during or following completion of cancer therapy, may vary with unique pathophysiology of specific tumor types. Microglia and macrophages are important components of the tumor microenvironment, and tumor-associated macrophages play complex roles in cancer pathophysiology and therapy, particularly in the context of immunotherapeutic strategies (Lin et al., 2018; Pyonteck et al., 2013; Quail et al., 2016).

Microglia Influence Neural Cell Populations in Health and in Disease

Microglial interactions with neural cell populations are important to neurodevelopment and homeostasis in health (Bialas and Stevens, 2013; Schafer et al., 2012) and are key cellular mediators of neural dysfunction in disease (Liddelow et al., 2017). In prenatal and early postnatal development, loss of microglia disrupts neural precursor cell fate choice, with increases in neurons and astrocytes and decreases in oligodendroglial cell populations (Erblich et al., 2011). Microglia regulate early postnatal myelinogenesis and oligodendroglial cell density in a white matter-specific manner and continue to influence OPC population maintenance in the healthy brain during adulthood (Hagemeyer et al., 2017; Janova et al., 2018). Here, our finding that MTX chemotherapy-induced microglial inflammation is central to the disruption of glial cell homeostasis after chemotherapy exposure is consistent with an emerging role for microglia in a range of nervous system diseases associated with myelin dysfunction, including catatonia (Janova et al., 2018), Alzheimer's disease (Dagher et al., 2015), and multiple sclerosis (Zrzavy et al., 2017). In support of the data presented here, previous work has shown that the chemotherapy drug combination of cyclophosphamide, MTX, and 5-FU (CMF) induces elevated inflammatory cytokines in the brains of aged rats that correlate with behavioral and myelin deficits (Briones and Woods, 2014).

Recently, neuroinflammatory microglia were shown to induce astrocyte reactivity. This reactivity can subsequently cause neuronal and oligodendrocyte cell death, as well as inhibit oligodendroglial differentiation (Liddelow et al., 2017). Consistently, we find that the ongoing neuroinflammatory microglial response following MTX chemotherapy exposure induces astrocytic reactivity. The persistent decrement in mature oligodendrocytes observed following chemotherapy exposure may therefore be a result of both incomplete OPC differentiation as well as reactive astrocyte-induced oligodendrocyte death. Microglia may thus influence oligodendroglial lineage cell function directly (Hagemeyer et al., 2017; Miron et al., 2013) or indirectly through neurotoxic astrocyte activation (Liddelow et al., 2017), illustrating a complex balance between these glial populations.

In addition to the demonstrated changes in microglial-macrophagial interactions, the interplay between neurons and glia following chemotherapy exposure remains to be fully determined. Chemotherapy exposure is associated with decreased dendritic spines and neuronal arborizations (Zhou et al., 2016),

although the relationship to microglial pathology has not yet been explored. In addition to neurotoxic influences of activated astrocytes on mature neurons (Liddelow et al., 2017), proinflammatory astrocytes have also recently been shown to decrease hippocampal neurogenesis (Garber et al., 2018). Healthy hippocampal astrocytes influence long-term potentiation of synaptic activity and memory allocation (Adamsky et al., 2018), and the extent to which astrocytic contributions to cognition are disrupted by proinflammatory activation following MTX chemotherapy is unknown. Alterations in the ability of oligodendroglia to metabolically support axons (Simons and Nave, 2015) following chemotherapy exposure also remain to be elucidated. Collectively, these studies suggest complex cellular interactions are central to changes in brain structure and function following chemotherapy.

Conclusions

Here we show that the persistence of methotrexate chemotherapy-related cognitive impairment is associated with tri-glia dysfunction of oligodendrocyte lineage cells, astrocytes, and microglia. Activation of microglia is necessary for this cellular and functional dysregulation. The complex interplay between glia underscores the importance of these cells in a range of pathologies. As microglial activation is necessary for this dysregulation, these findings suggest a potential therapeutic approach relying on CSF1R inhibitors, such as PLX5622, and similar agents currently in clinical trials for other indications. This work presents a promising therapeutic avenue to ameliorate the long-term neurological consequences of chemotherapy exposure, a debilitating syndrome that affects a great number of cancer survivors.

STAR METHODS

Detailed methods are provided in the online version of this paper and include the following:

- KEY RESOURCES TABLE
- CONTACT FOR REAGENT AND RESOURCE SHARING
- EXPERIMENTAL MODEL AND SUBJECT DETAILS
 - Human tissue analyses
 - Mouse Maintenance
 - Isolation of Cells from Mouse Brain and Human Pediatric Brain Tumors
- METHOD DETAILS
 - Liquid chromatography tandem mass spectrometry (LC-MS/MS)
 - Chemotherapy treatment paradigm
 - Perfusion and immunohistochemistry
 - RNAscope
 - Confocal imaging
 - Volume measures
 - Electron microscopy
 - IC₅₀ Testing
 - Syngeneic Transplantation of OPCs
 - Behavioral analysis
 - Microfluidic qRT-PCR
 - Standard qRT-PCR

- Depletion of microglia using PLX5622
- QUANTIFICATION AND STATISTICAL ANALYSIS
- DATA AND SOFTWARE AVAILABILITY
 - Data Resources

SUPPLEMENTAL INFORMATION

Supplemental Information includes five figures and two tables and can be found with this article online at <https://doi.org/10.1016/j.cell.2018.10.049>.

A video abstract is available at <https://doi.org/10.1016/j.cell.2018.10.049#mmc3>.

ACKNOWLEDGMENTS

We acknowledge support from the California Institute for Regenerative Medicine (CIRM RB4-06093 and RN3-06510), Unravel Pediatric Cancer, McKenna Claire Foundation, Virginia and D.K. Ludwig Fund for Cancer Research, National Institutes of Neurological Disorders and Stroke (R01NS092597), Stanford Medical Scientist Training Program, Stanford Neuroscience Institute, the Stanford Maternal and Child Health Research Institute, Anne T. and Robert M. Bass Endowed Faculty Scholarship in Pediatric Cancer and Blood Diseases, Stanford CTSA (UL1 RR025744), BioX Institute, McCormick Fellowship, Stanford MedScholars Program, Christopher and Dana Reeve Foundation, the Novartis Institute for Biomedical Research, Dr. Miriam and Sheldon G. Adelson Medical Research Foundation, the JPB Foundation, the Cure Alzheimer's Fund, the Glenn Foundation, the Esther B. O'Keeffe Charitable Foundation, Australian National Health and Medical Research Council (GNT1052961), and the Glenn Foundation Glenn Award. Special thanks to Sigrid Knemeyer for illustrations and Wenchao Sun for LC-MS/MS processing.

AUTHOR CONTRIBUTIONS

E.M.G. and M.M. contributed to experimental design. E.M.G. and M.M. wrote the manuscript. E.M.G. performed the data analysis for all sections and made all figures. L.S.W. and E.M.G. developed the MTX mouse model. E.M.G., L.S.W., and H.V. performed all human histological studies. S.L. and B.A.B. performed the astrocyte and microglial reactivity analyses. S.N. performed all FACS sorting and contributed to the RNAscope experiments. L.N. performed electron microscopy studies. E.M.G., A.K.G., A.O., P.N.P., J.J.G., L.T.T., A.C.G., and P.J.W. contributed to the execution of experiments. M.M. conceived of the project and supervised all aspects of the work.

DECLARATION OF INTERESTS

The authors declare no competing interests.

Received: May 30, 2018

Revised: September 12, 2018

Accepted: October 23, 2018

Published: December 6, 2018

REFERENCES

- Acharya, M.M., Martirosian, V., Chmielewski, N.N., Hanna, N., Tran, K.K., Liao, A.C., Christie, L.A., Parihar, V.K., and Limoli, C.L. (2015). Stem cell transplantation reverses chemotherapy-induced cognitive dysfunction. *Cancer Res.* 75, 676–686.
- Adamsky, A., Kol, A., Kreisel, T., Doron, A., Ozeri-Engelhard, N., Melcer, T., Refaeli, R., Horn, H., Regev, L., Groysman, M., et al. (2018). Astrocytic activation generates de novo neuronal potentiation and memory enhancement. *Cell* 174, 59–71.e14.
- American Cancer Society (2016). Cancer treatment & survivorship facts & figures 2016–2017. <https://www.cancer.org/research/cancer-facts-statistics/survivor-facts-figures.html>

- Anderson, V.A., Godber, T., Smibert, E., Weiskopf, S., and Ekert, H. (2000). Cognitive and academic outcome following cranial irradiation and chemotherapy in children: a longitudinal study. *Br. J. Cancer* 82, 255–262.
- Aukema, E.J., Caan, M.W., Oudhuis, N., Majoe, C.B., Vos, F.M., Reneman, L., Last, B.F., Grootenhuis, M.A., and Schouten-van Meeteren, A.Y. (2009). White matter fractional anisotropy correlates with speed of processing and motor speed in young childhood cancer survivors. *Int. J. Radiat. Oncol. Biol. Phys.* 74, 837–843.
- Baxi, E.G., DeBruin, J., Jin, J., Strasburger, H.J., Smith, M.D., Orthmann-Murphy, J.L., Schott, J.T., Fairchild, A.N., Bergles, D.E., and Calabresi, P.A. (2017). Lineage tracing reveals dynamic changes in oligodendrocyte precursor cells following cuprizone-induced demyelination. *Glia* 65, 2087–2098.
- Benes, F.M. (1989). Myelination of cortical-hippocampal relays during late adolescence. *Schizophr. Bull.* 15, 585–593.
- Bialas, A.R., and Stevens, B. (2013). TGF- β signaling regulates neuronal C1q expression and developmental synaptic refinement. *Nat. Neurosci.* 16, 1773–1782.
- Bisen-Hersh, E.B., Hineline, P.N., and Walker, E.A. (2013). Effects of early chemotherapeutic treatment on learning in adolescent mice: implications for cognitive impairment and remediation in childhood cancer survivors. *Clin. Cancer Res.* 19, 3008–3018.
- Bohlen, C.J., Bennett, F.C., Tucker, A.F., Collins, H.Y., Mulinyawe, S.B., and Barres, B.A. (2017). Diverse requirements for microglial survival, specification, and function revealed by defined-medium cultures. *Neuron* 94, 759–773.e8.
- Bratlid, D., and Moe, P.J. (1978). Pharmacokinetics of high-dose methotrexate treatment in children. *Eur. J. Clin. Pharmacol.* 14, 143–147.
- Bray, V.J., Dhillon, H.M., Bell, M.L., Kabourakis, M., Fiero, M.H., Yip, D., Boyle, F., Price, M.A., and Vardy, J.L. (2017). Evaluation of a web-based cognitive rehabilitation program in cancer survivors reporting cognitive symptoms after chemotherapy. *J. Clin. Oncol.* 35, 217–225.
- Briones, T.L., and Woods, J. (2014). Dysregulation in myelination mediated by persistent neuroinflammation: possible mechanisms in chemotherapy-related cognitive impairment. *Brain Behav. Immun.* 35, 23–32.
- Chung, W.S., Clarke, L.E., Wang, G.X., Stafford, B.K., Sher, A., Chakraborty, C., Joung, J., Foo, L.C., Thompson, A., Chen, C., et al. (2013). Astrocytes mediate synapse elimination through MEGF10 and MERTK pathways. *Nature* 504, 394–400.
- Dagher, N.N., Najafi, A.R., Kayala, K.M., Elmore, M.R., White, T.E., Medeiros, R., West, B.L., and Green, K.N. (2015). Colony-stimulating factor 1 receptor inhibition prevents microglial plaque association and improves cognition in 3xTg-AD mice. *J. Neuroinflammation* 12, 139.
- Dawson, M.R., Polito, A., Levine, J.M., and Reynolds, R. (2003). NG2-expressing glial progenitor cells: an abundant and widespread population of cycling cells in the adult rat CNS. *Mol. Cell. Neurosci.* 24, 476–488.
- Dietrich, J., Han, R., Yang, Y., Mayer-Pröschel, M., and Noble, M. (2006). CNS progenitor cells and oligodendrocytes are targets of chemotherapeutic agents *in vitro* and *in vivo*. *J. Biol.* 5, 22.
- Ellenberg, L., Liu, Q., Gioia, G., Yasui, Y., Packer, R.J., Mertens, A., Donaldson, S.S., Stovall, M., Kadan-Lottick, N., Armstrong, G., et al. (2009). Neurocognitive status in long-term survivors of childhood CNS malignancies: a report from the Childhood Cancer Survivor Study. *Neuropsychology* 23, 705–717.
- Elmore, M.R., Najafi, A.R., Koike, M.A., Dagher, N.N., Spangenberg, E.E., Rice, R.A., Kitazawa, M., Matusow, B., Nguyen, H., West, B.L., and Green, K.N. (2014). Colony-stimulating factor 1 receptor signaling is necessary for microglia viability, unmasking a microglia progenitor cell in the adult brain. *Neuron* 82, 380–397.
- Erblich, B., Zhu, L., Etgen, A.M., Dobrenis, K., and Pollard, J.W. (2011). Absence of colony stimulation factor-1 receptor results in loss of microglia, disrupted brain development and olfactory deficits. *PLoS ONE* 6, e26317.
- Foo, L.C., Allen, N.J., Bushong, E.A., Ventura, P.B., Chung, W.S., Zhou, L., Cahoy, J.D., Daneman, R., Zong, H., Ellisman, M.H., and Barres, B.A. (2011). Development of a method for the purification and culture of rodent astrocytes. *Neuron* 71, 799–811.
- Garber, C., Vasek, M.J., Vollmer, L.L., Sun, T., Jiang, X., and Klein, R.S. (2018). Astrocytes decrease adult neurogenesis during virus-induced memory dysfunction via IL-1. *Nat. Immunol.* 19, 151–161.
- Geha, S., Pallud, J., Junier, M.P., Devaux, B., Leonard, N., Chassoux, F., Chneiweiss, H., Daumas-Duport, C., and Varlet, P. (2010). NG2+/Olig2+ cells are the major cycle-related cell population of the adult human normal brain. *Brain Pathol.* 20, 399–411.
- Gibson, E., and Monje, M. (2012). Effect of cancer therapy on neural stem cells: implications for cognitive function. *Curr. Opin. Oncol.* 24, 672–678.
- Gibson, E.M., Purger, D., Mount, C.W., Goldstein, A.K., Lin, G.L., Wood, L.S., Inema, I., Miller, S.E., Bieri, G., Zuchero, J.B., et al. (2014). Neuronal activity promotes oligodendrogenesis and adaptive myelination in the mammalian brain. *Science* 344, 1252304.
- Grabert, K., Michoel, T., Karavolos, M.H., Clohisey, S., Baillie, J.K., Stevens, M.P., Freeman, T.C., Summers, K.M., and McColl, B.W. (2016). Microglial brain region-dependent diversity and selective regional sensitivities to aging. *Nat. Neurosci.* 19, 504–516.
- Green, J.L., Knight, S.J., McCarthy, M., and De Luca, C.R. (2013). Motor functioning during and following treatment with chemotherapy for pediatric acute lymphoblastic leukemia. *Pediatr. Blood Cancer* 60, 1261–1266.
- Hagemeyer, N., Hanft, K.M., Akriditou, M.A., Unger, N., Park, E.S., Stanley, E.R., Staszewski, O., Dimou, L., and Prinz, M. (2017). Microglia contribute to normal myelinogenesis and to oligodendrocyte progenitor maintenance during adulthood. *Acta Neuropathol.* 134, 441–458.
- Han, R., Yang, Y.M., Dietrich, J., Luebke, A., Mayer-Pröschel, M., and Noble, M. (2008). Systemic 5-fluorouracil treatment causes a syndrome of delayed myelin destruction in the central nervous system. *J. Biol.* 7, 12.
- Hill, R.A., Li, A.M., and Grutzendler, J. (2018). Lifelong cortical myelin plasticity and age-related degeneration in the live mammalian brain. *Nat. Neurosci.* 21, 683–695.
- Horowitz, T.S., Suls, J., and Treviño, M. (2018). A call for a neuroscience approach to cancer-related cognitive impairment. *Trends Neurosci.* 41, 493–496.
- Hughes, E.G., Kang, S.H., Fukaya, M., and Bergles, D.E. (2013). Oligodendrocyte progenitors balance growth with self-repulsion to achieve homeostasis in the adult brain. *Nat. Neurosci.* 16, 668–676.
- Hughes, E.G., Orthmann-Murphy, J.L., Langseth, A.J., and Bergles, D.E. (2018). Myelin remodeling through experience-dependent oligodendrogenesis in the adult somatosensory cortex. *Nat. Neurosci.* 21, 696–706.
- Hyrien, O., Dietrich, J., and Noble, M. (2010). Mathematical and experimental approaches to identify and predict the effects of chemotherapy on neuroglial precursors. *Cancer Res.* 70, 10051–10059.
- Janova, H., Arinrad, S., Balmuth, E., Mitjans, M., Hertel, J., Habes, M., Bittner, R.A., Pan, H., Goebels, S., Begemann, M., et al. (2018). Microglia ablation alleviates myelin-associated catatonic signs in mice. *J. Clin. Invest.* 128, 734–745.
- Lebel, C., Gee, M., Camicioli, R., Wieler, M., Martin, W., and Beaulieu, C. (2012). Diffusion tensor imaging of white matter tract evolution over the life-span. *Neuroimage* 60, 340–352.
- Leger, M., Quiedeville, A., Bouet, V., Haelewyn, B., Boulouard, M., Schumann-Bard, P., and Freret, T. (2013). Object recognition test in mice. *Nat. Protoc.* 8, 2531–2537.
- Liddelow, S.A., Guttenplan, K.A., Clarke, L.E., Bennett, F.C., Bohlen, C.J., Schirmer, L., Bennett, M.L., Münch, A.E., Chung, W.S., Peterson, T.C., et al. (2017). Neurotoxic reactive astrocytes are induced by activated microglia. *Nature* 541, 481–487.
- Lin, G.L., Nagaraja, S., Filbin, M.G., Suvà, M.L., Vogel, H., and Monje, M. (2018). Non-inflammatory tumor microenvironment of diffuse intrinsic pontine glioma. *Acta Neuropathol. Commun.* 6, 51.
- McKenzie, I.A., Ohayon, D., Li, H., de Faria, J.P., Emery, B., Tohyama, K., and Richardson, W.D. (2014). Motor skill learning requires active central myelination. *Science* 346, 318–322.

- Miron, V.E., Kuhlmann, T., and Antel, J.P. (2011). Cells of the oligodendroglial lineage, myelination, and remyelination. *Biochim. Biophys. Acta* **1812**, 184–193.
- Miron, V.E., Boyd, A., Zhao, J.W., Yuen, T.J., Ruckh, J.M., Shadrach, J.L., van Wijngaarden, P., Wagers, A.J., Williams, A., Franklin, R.J.M., and Ffrench-Constant, C. (2013). M2 microglia and macrophages drive oligodendrocyte differentiation during CNS remyelination. *Nat. Neurosci.* **16**, 1211–1218.
- Mitew, S., Gobius, I., Fenlon, L.R., McDougall, S.J., Hawkes, D., Xing, Y.L., Bujalka, H., Gundlach, A.L., Richards, L.J., Kilpatrick, T.J., et al. (2018). Pharmacogenetic stimulation of neuronal activity increases myelination in an axon-specific manner. *Nat. Commun.* **9**, 306.
- Monje, M.L., Mizumatsu, S., Fike, J.R., and Palmer, T.D. (2002). Irradiation induces neural precursor-cell dysfunction. *Nat. Med.* **8**, 955–962.
- Monje, M.L., Toda, H., and Palmer, T.D. (2003). Inflammatory blockade restores adult hippocampal neurogenesis. *Science* **302**, 1760–1765.
- Monje, M.L., Vogel, H., Masek, M., Ligon, K.L., Fisher, P.G., and Palmer, T.D. (2007). Impaired human hippocampal neurogenesis after treatment for central nervous system malignancies. *Ann. Neurol.* **62**, 515–520.
- Monje, M., Mitra, S.S., Freret, M.E., Raveh, T.B., Kim, J., Masek, M., Attema, J.L., Li, G., Haddix, T., Edwards, M.S., et al. (2011). Hedgehog-responsive candidate cell of origin for diffuse intrinsic pontine glioma. *Proc. Natl. Acad. Sci. USA* **108**, 4453–4458.
- Moore, B.D., 3rd, Copeland, D.R., Ried, H., and Levy, B. (1992). Neurophysiological basis of cognitive deficits in long-term survivors of childhood cancer. *Arch. Neurol.* **49**, 809–817.
- Morioka, S., Morimoto, M., Yamada, K., Hasegawa, T., Morita, T., Moroto, M., Isoda, K., Chiyonobu, T., Immura, T., Nishimura, A., et al. (2013). Effects of chemotherapy on the brain in childhood: diffusion tensor imaging of subtle white matter damage. *Neuroradiology* **55**, 1251–1257.
- Morris, G.M., Hopewell, J.W., and Morris, A.D. (1995). A comparison of the effects of methotrexate and misonidazole on the germinal cells of the subependymal plate of the rat. *Br. J. Radiol.* **68**, 406–412.
- Mount, C.W., and Monje, M. (2017). Wrapped to adapt: experience-dependent myelination. *Neuron* **95**, 743–756.
- Parent, J.M., Tada, E., Fike, J.R., and Lowenstein, D.H. (1999). Inhibition of dentate granule cell neurogenesis with brain irradiation does not prevent seizure-induced mossy fiber synaptic reorganization in the rat. *J. Neurosci.* **19**, 4508–4519.
- Pierson, C., Waite, E., and Pykkonen, B. (2016). A meta-analysis of the neuropsychological effects of chemotherapy in the treatment of childhood cancer. *Pediatr. Blood Cancer* **63**, 1998–2003.
- Pyonteck, S.M., Akkari, L., Schuhmacher, A.J., Bowman, R.L., Sevenich, L., Quail, D.F., Olson, O.C., Quick, M.L., Huse, J.T., Teijeiro, V., et al. (2013). CSF-1R inhibition alters macrophage polarization and blocks glioma progression. *Nat. Med.* **19**, 1264–1272.
- Quail, D.F., Bowman, R.L., Akkari, L., Quick, M.L., Schuhmacher, A.J., Huse, J.T., Holland, E.C., Sutton, J.C., and Joyce, J.A. (2016). The tumor microenvironment underlies acquired resistance to CSF-1R inhibition in gliomas. *Science* **352**, aad3018.
- Robinson, G.W., Rudneva, V.A., Buchhalter, I., Billups, C.A., Waszak, S.M., Smith, K.S., Bowers, D.C., Bendel, A., Fisher, P.G., Partap, S., et al. (2018). Risk-adapted therapy for young children with medulloblastoma (SJYC07): therapeutic and molecular outcomes from a multicentre, phase 2 trial. *Lancet Oncol.* **19**, 768–784.
- Schafer, D.P., Lehrman, E.K., Kautzman, A.G., Koyama, R., Mardini, A.R., Yamasaki, R., Ransohoff, R.M., Greenberg, M.E., Barres, B.A., and Stevens, B. (2012). Microglia sculpt postnatal neural circuits in an activity and complement-dependent manner. *Neuron* **74**, 691–705.
- Seigers, R., Schagen, S.B., Coppens, C.M., van der Most, P.J., van Dam, F.S., Koolhaas, J.M., and Buwalda, B. (2009). Methotrexate decreases hippocampal cell proliferation and induces memory deficits in rats. *Behav. Brain Res.* **201**, 279–284.
- Seigers, R., Timmermans, J., van der Horn, H.J., de Vries, E.F., Dierckx, R.A., Visser, L., Schagen, S.B., van Dam, F.S., Koolhaas, J.M., and Buwalda, B. (2010). Methotrexate reduces hippocampal blood vessel density and activates microglia in rats but does not elevate central cytokine release. *Behav. Brain Res.* **207**, 265–272.
- Simons, M., and Nave, K.A. (2015). Oligodendrocytes: myelination and axonal support. *Cold Spring Harb. Perspect. Biol.* **8**, a020479.
- Tripathi, R.B., Jackiewicz, M., McKenzie, I.A., Kougioumtzidou, E., Grist, M., and Richardson, W.D. (2017). Remarkable Stability of Myelinating Oligodendrocytes in Mice. *Cell Rep.* **21**, 316–323.
- Viganò, F., Möbius, W., Götz, M., and Dimou, L. (2013). Transplantation reveals regional differences in oligodendrocyte differentiation in the adult brain. *Nat. Neurosci.* **16**, 1370–1372.
- Wefel, J.S., and Schagen, S.B. (2012). Chemotherapy-related cognitive dysfunction. *Curr. Neurol. Neurosci. Rep.* **12**, 267–275.
- Winocur, G., Vardy, J., Binns, M.A., Kerr, L., and Tannock, I. (2006). The effects of the anti-cancer drugs, methotrexate and 5-fluorouracil, on cognitive function in mice. *Pharmacol. Biochem. Behav.* **85**, 66–75.
- Xiao, L., Ohayon, D., McKenzie, I.A., Sinclair-Wilson, A., Wright, J.L., Fudge, A.D., Emery, B., Li, H., and Richardson, W.D. (2016). Rapid production of new oligodendrocytes is required in the earliest stages of motor-skill learning. *Nat. Neurosci.* **19**, 1210–1217.
- Yakovlev, P. (1967). The myelogenetic cycles of regional maturation of the brain. In *Regional Development of the Brain in Early Life* Oxford, A. Minkowski, ed. (Blackwell Scientific Publications), pp. 3–70.
- Yang, Y., Vidensky, S., Jin, L., Jie, C., Lorenzini, I., Frankl, M., and Rothstein, J.D. (2011). Molecular comparison of GLT1+ and ALDH1L1+ astrocytes in vivo in astrogli reporter mice. *Glia* **59**, 200–207.
- Zamanian, J.L., Xu, L., Foo, L.C., Nouri, N., Zhou, L., Giffard, R.G., and Barres, B.A. (2012). Genomic analysis of reactive astrogliosis. *J. Neurosci.* **32**, 6391–6410.
- Zhou, W., Kavelaars, A., and Heijnen, C.J. (2016). Metformin prevents cisplatin-induced cognitive impairment and brain damage in mice. *PLoS ONE* **11**, e0151890.
- Zrzavy, T., Hametner, S., Wimmer, I., Butovsky, O., Weiner, H.L., and Lassmann, H. (2017). Loss of ‘homeostatic’ microglia and patterns of their activation in active multiple sclerosis. *Brain* **140**, 1900–1913.

STAR★METHODS

KEY RESOURCES TABLE

REAGENT OR RESOURCE	SOURCE	IDENTIFIER
Antibodies		
CD45	PharMingen BD	Cat# 550539; RRID: AB_2174426
Lectin BSL-1	Vector Labs	Cat# L-1100; RRID: AB_2336491
Mouse monoclonal anti-ITGB5	eBioscience	Cat# 14-0497-82; RRID: AB_467288
Goat anti-mouse IgG (H+L)	Jackson ImmunoResearch	Cat# 115-005-003; RRID: AB_2338447
Rat monoclonal anti-mouse CD45	eBioscience	Cat# 25-0451-82; RRID: AB_469625
Rat anti-mouse CD45	BD PharMingen	Cat# 550539
Goat anti-mouse IgM μ -chain	Jackson ImmunoResearch	Cat# 115-005-02
Goat anti-mouse IgG+IgM (H+L)	Jackson ImmunoResearch	Cat# 115-005-044
O4 hybridoma supernatant mouse IgM	Foo et al., 2011	N/A
Bovine serum albumin	Sigma	Cat# A4161
Mouse anti-human Olig2, clone 211F1.1	Cell Marque	Cat# 387M-16
Mouse anti-human Nestin, clone 10C2	EMD Millipore	Cat# MAB5326
Rat IgG	R&D Systems	Cat# 6-001-A
Mouse anti-CD140a	BioLegend	Cat# 135902; RRID: AB_1953328
Mouse/Human anti-CD11b	BioLegend	Cat# 101216; RRID: AB_312799
Near IR LIVE/DEAD	Life Technologies	Cat# L10119
Goat anti-PDGFR α	R&D Systems	Cat# AF1062
Rabbit anti-Iba1	Wako	Cat# 019-19741; RRID: AB_839504
Rat anti-CD68	Abcam	Cat# AB53444; RRID: AB_869007
Mouse anti-CC1	Millipore	Cat# OP-80; RRID: AB_2057371
Rabbit anti-cleaved caspase3	Cell Signaling	Cat# 9661S; RRID AB_2341188
Rat anti-MBP	Abcam	Cat# AB7349; RRID AB_305869
Rabbit anti-NGS	Sigma	Cat# HPA002951; RRID AB_1854449
Chemicals, Peptides, and Recombinant Proteins		
Human TGF- b2	Peprotech	Cat# 100-35B
Murine IL-34	R&D Systems	Cat# 5195-ML/CF
Ovine wool cholesterol	Avanti Polar Lipids	Cat# 700000P
Ovomucoid trypsin inhibitor	Worthington	Cat# LS003086
DNaseI	Worthington	Cat# DPRFS
Percoll PLUS	GE Healthcare	Cat# 17-5445-02
Trypsin	Sigma	Cat# T9935
DMEM/F12	GIBCO	Cat# 21041-02
Penicillin/ Streptomycin	GIBCO	Cat# 15140-122
Glutamine	GIBCO	Cat# 25030-081
N-acetyl cysteine	Sigma	Cat# A9165
Insulin	Sigma	Cat# I6634
Sodium selenite	Sigma	Cat# S-5261
Papain	Worthington	Cat# LS003126
DMEM (high glucose)	GIBCO	Cat# 11960-044
Neurobasal	GIBCO	Cat# 21103-049
Sodium pyruvate	Sigma	Cat# P5280
Hydrocortisone	Sigma	Cat# H0888
Forskolin	Sigma	Cat# F6886

(Continued on next page)

Continued

REAGENT OR RESOURCE	SOURCE	IDENTIFIER
Putrescine	Sigma	Cat# P-5780
Progesterone	Sigma	Cat# P-8783
SYBR Green PCR Master Mix	Thermo Fisher	Cat# 4385612
TaqMan PreAmp Master Mix Kit	Applied Biosystems	Cat# 4384267
TE Buffer	Technova	Cat# T0225
96.96 Dynamic Array chip	Fluidigm	Cat# BMK-M-96.96
Recombinant Human HBEGF	Peprotech	Cat# 100-47
Apo-transferrin	Sigma	Cat# T1147
DMSO DMSO, Anhydrous	Thermo Fisher	Cat# D12345
Earle's balanced salt solution	Sigma	Cat# E7510
Fetal calf serum	GIBCO	Cat# 10437-028
Dulbecco's PBS (dPBS)	GIBCO	Cat# 14040182
Neurobasal(-A)	Invitrogen	Cat#10888-022
Antibiotic-antimycotic	Invitrogen	Cat#15240096
Epidermal Growth Factor	Life Technologies	Cat# E-35351
B27(-A)	Invitrogen	Cat# 12587010
Fibroblast Growth Factor	PeproTech	Cat# 450-33
heparin	Stem Cell Technologies	Cat# 07980
Human-bFGF	Shenandoah Biotech	Cat# 100-146
Human-EGF	Shenandoah Biotech	Cat# 100-26
Human PDGF-AA	Shenandoah Biotech	Cat# 100-16
Human PDGF-BB	Shenandoah Biotech	Cat# 100-18
Liberase-H	Roche	Cat# 05401054001
5-ethynyl-2'-deoxyuridine (EdU)	Invitrogen	Cat# E10187
Click-iT EdU kit	Thermo Fisher	Cat# C10424
Slc1a3	Advanced Cell Diagnostics	Cat# 430781
Cxcl10	Advanced Cell Diagnostics	Cat# 408921-C2
Glutaraldehyde	EMS	Cat# 16000
Paraformaldehyde	EMS	Cat# 15700
Sodium cacodylate	EMS	Cat# 12300
Embed-812 resin	EMS	Cat# 14120
CellTiter-Glo	Promega	Cat# G9243
Glutamax	Invitrogen	Cat# 35050-061
Sodium pyruvate	Thermo Fisher	Cat# 11360070
MEM NEAAAs	Invitrogen	Cat# 11140050
N21-MAX	R&D Systems	Cat# AR012
Trace Elements B	Corning	Cat# 25-022-Cl
Insulin	Sigma	Cat# 19278
N-acetyl cystein	Sigma	Cat# A9165
PDGF-AA	PeproTech	Cat# 315-17
CNTF	PeproTech	Cat# 450-13
NT-3	PeproTech	Cat# 450-03
Critical Commercial Assays		
RNeasy Micro Kit	QIAGEN	Cat# 74004
High-Capacity RNA-to-cDNA Kit	Thermo Fisher	Cat# 4387406
RNAScope Fluorescent Multiplex Reagent Kit	Advanced Cell Diagnostics	Cat# 320850

(Continued on next page)

Continued

REAGENT OR RESOURCE	SOURCE	IDENTIFIER
Experimental Models: Organisms/Strains		
Mouse: CD57BL/6	Charles River	Cat# 027
Mouse: CD1	Charles River	Cat# 022
Mouse: C57BL/6-Tg(CAG-EGFP)1Osb/J	The Jackson Laboratory	Cat# 003291
Rat: Sprague-Dawley	Charles River	Cat# 400
Oligonucleotides		
Primers for qPCR and microfluidic qPCR	See Table S2	N/A
Primers for qPCR and microfluidic qPCR	See Table S2	N/A
Software and Algorithms		
ImageJ	NIH	N/A
Incucyte ZOOM	Essen Bioscience	N/A
BioMark™ Data Collection Software 2.1.1 build 20090519.0926	Fluidigm	N/A
Fluidigm Melting Curve Analysis Software 1.1.0 build 20100514.1234	Fluidigm	N/A
Real-time PCR Analysis Software 2.1.1 build 20090521.1135	Fluidigm	N/A
Mastercycler ep realplex v2.2	Eppendorf	N/A
Analyst 1.6.1 Software	AB SCIEX	N/A
Other		
Dounce homogenizer	Wheaton	Cat# 357424

CONTACT FOR REAGENT AND RESOURCE SHARING

Further information and requests for resources and reagents should be directed to and will be fulfilled by the Lead Contact, Michelle Monje (mmonje@stanford.edu).

EXPERIMENTAL MODEL AND SUBJECT DETAILS**Human tissue analyses**

Human samples were collected as part of a routine autopsy protocol from a standardized location of frontal cortex/subcortical white matter in individuals treated with multi-agent chemotherapy during childhood/young adulthood and from age-matched, non-chemotherapy exposed control cases. No cases received cerebral radiotherapy. Samples were obtained in collaboration with the Department of Pathology at Stanford University (see Table S1). FFPE samples were stained immunohistochemically according to standard procedures on paraffin embedded sections (5 µm) (Monje et al., 2011). A control stain of Nestin was used to ensure quality of tissue samples. The following antibodies were used: Olig-2 (1:100, Cell Marque, 387M-16) and Nestin (1:20000, Millipore, MAB5326). For each sample, 200X frames were captured using a Nikon Eclipse E1000 microscope with a SPOT Flex camera in both gray matter and white matter regions, for a total of 10 images/case. The total density of Olig2⁺ cells was determined by extrapolating number of Olig2⁺ cells by the total volume of tissue assessed. For fluorescent immunohistochemistry, frontal lobe samples from both cases were obtained as part of a rapid autopsy protocol for tumor tissue donation, fixed in 4% paraformaldehyde and embedded in 30% sucrose. Tissue was then sectioned at 40 µm and processed for confocal microscopy as described below. Tissue was processed with goat anti-PDGFR α (1:250, R&D Systems, AF1062) and rabbit anti-NG2 (1:200, Sigma, HPA002951) and imaged at 400X using a Zeiss LSM 700. All human tissue studies were performed with informed consent and in accordance with Institutional Review Board (IRB)-approved protocols.

Mouse Maintenance

Wild-type CD57BL/6 mice (Charles River) were bred with CD1 mice (Charles River) for all experiments unless otherwise noted. All animals were housed in a 12-hour light:dark cycle with *ad libitum* access to food and water. Animals were housed 2-5 per cage. Both sexes were used equally for all studies. No animals were manipulated other than as reported for that experimental group, i.e., there was no history of drug exposures, surgeries or behavioral testing for the animals used other than that reported for the given experimental group. All procedures were performed in accordance with guidelines set in place by the Stanford University Institutional Care and Use Committee.

Isolation of Cells from Mouse Brain and Human Pediatric Brain Tumors

Cell Culture for IC₅₀

Neural precursor cells (NPCs) were cultured as followed: Base cell medium for neural precursor cells was made using Neurobasal(-A) (Invitrogen, 10888-022), antibiotic-antimycotic (Invitrogen, 15240096), and B27(-A) (Invitrogen, 12587010). Mouse neural precursor cells (NPCs) of low passage number (10-15) were acquired. These cells were thawed from -80°C in a 37°C water bath and transferred to a 15 mL centrifuge tube where 10 mL of Hank's Balanced Salt Solution without Calcium and Magnesium (HBSS, Fisher Scientific) was added to dilute the cryogenic protecting agent, DMSO. Cells were centrifuged for 5 min (300 g). The supernatant was removed and replaced with 10 mL of base cell medium. This cell mixture was transferred to a T75cm² flask (Nunc™ Cell Culture Treated 75 cm² EasYFlask™, Fisher Scientific) along with Epidermal Growth Factor (at 20 ng/mL complexed to Alexa Fluor 647 Streptavidin, Life Technologies, E-35351), Fibroblast Growth Factor (20 ng/mL Streptavidin, PeproTech, 450-33), and heparin (2 ng/mL, Stem Cell Technologies, 07980). The NPCs were then used for IC₅₀ experiments. Mouse OPCs were obtained by FACS (see below) and cultured in DMEM with Glutamax (Invitrogen, 35050-061), sodium pyruvate (Thermo Fisher, 11360070), MEM NEAA (Invitrogen, 11140050), antibiotic-antimycotic with N21-MAX (R&D systems, AR012) and Trace Elements B (Corning, 25-022-CI) (all the aforementioned supplemented to 1X) and Insulin (5 µg/mL, Sigma, 19278), N-acetyl cysteine (5 µg/mL, Sigma, A9165), PDGFAA (10 ng/mL, PeproTech, 315-17), CNTF (10 ng/mL, PeproTech, 450-13), and NT-3 (1 ng/mL, PeproTech, 450-03). OPCs were then used for IC₅₀ experiments. Pediatric cortical glioblastoma (SU-PCGBM) and diffuse intrinsic pontine glioma IV (SU-DIPG IV) maintained in our lab were acquired. The SU-PCGBM and SU-DIPG IV cells were cultured in a T75cm² flask (Nunc™ Cell Culture Treated 75 cm² EasYFlask™, Fisher Scientific). A defined, serum-free medium designated "Tumor Stem Media (TSM)" was used throughout, consisting of Neurobasal(-A), B27(-A), human-bFGF (20 ng/mL, Shenandoah Biotech, 100-146), human-EGF (20 ng/mL, Shenandoah Biotech, 100-26), human PDGF-AA (10 ng/mL) and PDGF-BB (10 ng/mL) (Shenandoah, Biotech, 100-16 and 100-18) and heparin (2 ng/mL). When neurospheres and minimal space between growing cells were visible in the primary culture, the concentration of each cell line was determined using a hemocytometer (Hausser Scientific, Horsham, PA). NPCs were passaged every 4 days while SU-PCGBM and SU-DIPG IV cells were passaged every 2 weeks.

Isolation of OPCs, microglia, and astrocytes by fluorescence-activated cell sorting (FACS)

For OPC transplantation sorts or OPC IC₅₀, whole forebrains were removed from P6-8 GFP⁺ (C57BL/6-Tg(CAG-EGFP)1Osb/J; The Jackson Laboratory) or CD57BL/6:CD1 mice pups, respectively, of both sexes. For microglia and astrocyte sorts, frontal deep cortex and subjacent corpus callosum was microdissected from P63-65 mice. Tissue was then minced in Hibernate-A to approximately 1 mm³ pieces and pelleted at 200xg for 2 min. Supernatant was removed and tissue was resuspended in 25 µg/mL Liberase-H (Roche, 05401054001) solution in HBSS with Ca²⁺/Mg²⁺. Tissue was enzymatically dissociated for 30 min, rotating at 37°C. Samples were then triturated, and passed through a 100 µm filter. Dissociated tissue was pelleted then resuspended in 30% sucrose/HBSS solution and centrifuged at 2000 rpm for 10 min at 4°C without brake to remove myelin debris. Pellets were washed once in cold HBSS without Ca²⁺/Mg²⁺ and resuspended in Neurobasal-A + Hoechst 33342 (10 µg/ml final). Cells were then incubated at 37°C for 30 min to label nuclei. Samples were pelleted and resuspended in FACS Buffer (2% BSA/HBSS + 10 mM HEPES). Samples were blocked using rat IgG (8 µg/mL final, R&D Systems, 6-001-A) for 10 min on ice and then stained with preconjugated antibodies for 30 to 45 min. For OPC sorts, cells were stained with anti-CD140a (APA5, BioLegend, 135902). For microglial sorts, anti-CD11b (M1/70, BioLegend, 101216) was used. For astrocyte sorts, ALDH1L1-eGFP reporter mice were used (*Tg(Aldh1l1-eGFP) OFC789Gsat/Mmucl* mice were backcrossed onto a C57BL/6 black background (Chung et al., 2013) a gift from the B. Barres and S. Liddelow).

Antibody stains were washed out and cells were resuspended in cold HBSS with 1:1000 Near IR LIVE/DEAD (Life Technologies, L10119). Following a 20 to 30 min incubation on ice to label dead cells, samples were washed once with cold HBSS, resuspended in FACS Buffer, and sorted on a BD FACS Aria by sequential yield and purity sorts. OPCs were isolated as the CD140a⁺ (PDGFR α ⁺) population, microglia as the CD11b⁺ population, and astrocytes as the eGFP⁺ population. Microglia and astrocytes were sorted directly in RLT Plus Lysis Buffer.

Immunopanning and cell culture

Astrocytes were purified by immunopanning from P5 rat (Sprague Dawley rats obtained from Charles River) forebrains of both sexes and cultured as previously described (Foo et al., 2011). Briefly, cortices were enzymatically (papain) then mechanically dissociated to generate a single cell suspension that was incubated on successive negative immunopanning plates to remove microglia, endothelial cells, and oligodendrocyte lineage cells before positively selecting for astrocytes with an Itgb5-coated panning plate. Isolated astrocytes were cultured in a defined, serum-free base medium containing 50% neurobasal, 50% DMEM, 100 U/mL penicillin, 100 µg/mL streptomycin, 1 mM sodium pyruvate, 292 µg/mL L-glutamine, 1X SATO and 5 µg/mL of N-acetyl cysteine. This medium was supplemented with the astrocyte-required survival factor HBEGF (Peprotech, 100-47) at 5ng/mL as previously described (Foo et al., 2011). Microglia were purified by dounce homogenization on ice and grown in serum-free base medium containing DMEM/F12 containing 100 units/mL penicillin, 100 mg/mL streptomycin, 2mM glutamine, 5 mg/ml N-acetyl cysteine, 5 mg/mL insulin, 100 mg/mL apo-transferrin, and 100 ng/mL sodium selenite, all from GIBCO or Sigma. This medium was supplemented with the microglia-required survival factors: human TGF β 2 (2 ng/mL, Peprotech), murine IL34 (100 ng/mL, R&D Systems), and ovine wool cholesterol (1.5 mg/mL, Avanti Polar Lipids) (Bohlen et al., 2017). Both astrocyte and microglia cultures were treated with methotrexate dissolved in DMSO for 24 hr, before collection and microfluidic analysis of activation (see below).

METHOD DETAILS

Liquid chromatography tandem mass spectrometry (LC-MS/MS)

Blood, kidney, liver, and frontal cortex were acquired 30 min post a single 100 mg/kg methotrexate injection from 5 mice. Mice were transcardially perfused with cold PBS followed by tissue sample dissection. Tissues samples were weighed and 1 volume of bullet blender beads (Next Advance) and 3 volume of Milli-Q water were added. Tissues were homogenized by a bullet blender (Next Advance) at 4°C according to manufacturer's instruction. The neat stock solution of MTX was dissolved in DMSO at 5 mg/mL and further diluted in 50% methanol to prepare spiking solutions. To prepare spiked calibration curve, 25 µL of MTX spiking solutions (1-200 ng/mL for brain samples and 0.2-50 µg/ml for serum, kidney and liver samples) was mixed with 25 µL of blank tissue homogenate or serum. To prepare samples, the spiking solution was replaced by 25 µL of 50% methanol to make up the volume. After vortexing all standards and samples, 150 µL of methanol/acetonitrile 20:80 (v/v) containing the internal standard MTX-d3 was added to the mixture and vortexed vigorously for 1 min followed by centrifugation at 3,000 g for 10 min. The supernatant was diluted 3 times in Milli-Q water with 0.1% formic acid for brain samples and 50 times in 25% methanol with 0.1% formic acid for serum, kidney and liver samples.

The LC-MS/MS system consisted of a QTRAP 4000 mass spectrometer (AB SCIEX) coupled to a Shimadzu UFLC system. LC separation was carried out on an Acclaim 120 C8 column (2.1 mm × 50 mm, 5 µm) (Dionex) at room temperature. The analysis time was 2.6 min. The injection volume was 10 µL. The flow rate was 0.3 mL/min. Mobile phase A consisted of 2 mM ammonium acetate and 0.2% formic acid in LCMS grade water. Mobile phase B consisted of 0.1% formic acid in LCMS grade acetonitrile. The HPLC elution program was as follows: 10% B (0.5 min) → 40% B (linear increase in 1 min) → 10% B (linear decrease in 0.1 min) → 10% B (1 min). The mass spectrometer was operated in the positive mode with multiple-reaction monitoring (MRM) with the transition m/z 455.2 → 175.1 for MTX and m/z 458.2 → 311.1 for MTX-d3. Data acquisition and analysis were performed using the Analyst 1.6.1 software (AB SCIEX).

Chemotherapy treatment paradigm

CD57BL/6:CD1 mice were given an i.p. injection of 100 mg/kg methotrexate (MTX) dissolved in PBS obtained from the pharmacy at Lucile Packard Children's Hospital at Stanford University on P21, P28, and P35. For assessment of the effect of chemotherapy on proliferation, animals additionally received i.p. injections of the thymidine analog 5-ethynyl-2'-deoxyuridine (EdU; 40 mg/kg, Invitrogen, E10187) on P61, P62, and P63. Animals were then sacrificed (30 min post EdU injection) or assessed (see below) on P63 or P203.

Perfusion and immunohistochemistry

Animals assessed using fluorescent immunohistochemistry were anesthetized with avertin and transcardially perfused with 10-15 mL PBS. Brains were post-fixed in 4% paraformaldehyde (PFA) overnight at 4°C prior to cryoprotection in 30% sucrose. Brains were embedded in O.C.T. (Tissue-Tek) and sectioned at 40 µm in the coronal plane using a sliding microtome (Leica, HM450). For immunohistochemistry involving EdU, sections were stained using the Click-iT EdU cell proliferation kit (Thermo Fisher, C10424) and protocol to expose EdU labeling prior to blocking. For all other stains, sections were incubated directly in blocking solution (3% normal donkey serum, 0.3% Triton X-100 in TBS) for 1 hr at room temperature and then incubated in primary antibodies overnight. Goat anti-PDGFR α (1:500; R&D Systems AF1062), rabbit anti-Iba1 (1:2000; Wako 019-19741), rat anti-CD68 (1:200; Abcam AB53444), rabbit anti-Olig1 and mouse anti-Olig1 (1:5000; 1:500, respectively, a generous gift from Dr. John Alberta), mouse anti-CC1 (1:20 and incubated for 7-10 days; Millipore OP-80), rabbit anti-cleaved caspase-3 (1:500; Cell Signaling 9661S) and rat anti-MBP (1:200; Abcam AB7349) were diluted in 1% solution (1% normal donkey serum, 0.3% Triton X-100 in TBS) and incubated overnight at 4°C. All antibodies have been validated in the literature and/or in Antibodypedia for use in mouse immunohistochemistry. To further validate the antibodies in our hands, we confirmed that each antibody stained in the expected cellular patterns and brain-wide distributions. Secondary-only stains were performed as negative controls. The following day, sections were rinsed 3 times in 1X TBS and incubated in secondary antibody solution (1:500) and DAPI (1:1000) in 1% solution at 4°C overnight. The following secondary antibodies were used, Alexa 488 donkey anti-goat (Jackson ImmunoResearch), Alexa 594 donkey anti-goat (Jackson ImmunoResearch), Alexa 647 donkey anti-mouse (Invitrogen) or Alexa 647 donkey anti-rabbit (Jackson ImmunoResearch). The next day, sections were rinsed 3 times in TBS and mounted with Prolong Gold plus DAPI mounting medium (Invitrogen).

RNAScope

Animals were sacrificed at P62-64 and perfused with HBSS. Brains were removed and immediately placed in OCT and frozen in liquid nitrogen. Tissue was stored at -80°C until sectioned on a cryostat at a thickness of 16 µm. Before performing RNA Scope, slides were transferred directly from -80°C to 4% PFA/HBSS on ice for 15 min. Sections were then successively dehydrated in 50% ethanol, 70% ethanol, and twice in 100% ethanol for 5 min each and allowed to dry before treatment for 5 min with Protease IV from the RNA Scope Fluorescent Multiplex Reagent Kit (Advanced Cell Diagnostics, 320850). Slides were washed twice with HBSS before proceeding to probe hybridization. RNA Scope was performed according to Fluorescent Multiplex Reagent Kit protocol using RNA Scope probes against *Slc1a3* (*Glast*; Advanced Cell Diagnostics, 430781) and *Cxcl10* (Advanced Cell Diagnostics, 408921-C2). Slides were mounted in Prolong Gold and imaged on either a Zeiss LSM700 or LSM800 at 400X magnification within 72 hr of

hybridization. Z stacks were acquired for three counting frames throughout the corpus callosum of the frontal cortex and a maximum intensity image was generated for each image. The number of *Cxcl10* puncta per *Glast*⁺ cell was quantified by a blind rater for each image. Those *Glast*⁺ astrocytes with more than 8 *Cxcl10* puncta/cell were considered pan-reactive.

Confocal imaging

For fluorescent immunohistochemistry, two representative sections, one anterior and one posterior to the formation of the genu of the corpus callosum were selected for each animal. Z stacks were acquired using a Zeiss LSM 700 or LSM 800 for five counting frames taken at 200X (320 μm x 320 μm frame) between the two sections and a maximum intensity image was generated for each image. For each section, a superficial frame was captured to include layers I and II of the premotor cortex (M2) and a deep cortical frame was captured to include layers V and VI of the premotor cortex. For the white matter quantification, each section was imaged at the cingulum of the corpus callosum and half-way to midline within the corpus callosum. The posterior section included a frame taken at the genu of the corpus callosum.

Volume measures

Estimated volume measurements for the corpus callosum were obtained using the Cavalieri Estimator function on a MBF Bioscience StereoInvestigator version 11.01.2. A 1:6 series of coronal brain sections were stained with MBP antibody (myelin basic protein). Using the 10X objective, the Cavalieri Estimator probe was used to trace the corpus callosum; the boundaries were determined using published mouse anatomical guides. A total of 13 sections were analyzed per treatment group.

Electron microscopy

Four weeks (P63) or 6 months (P203) after the cessation of treatment, mice were sacrificed by transcardial perfusion with Karnovsky's fixative: 2% glutaraldehyde (EMS 16000) and 4% paraformaldehyde (EMS 15700) in 0.1M sodium cacodylate (EMS 12300), pH 7.4. Region containing premotor cortex (M2) and projections to the corpus callosum was resected from the brain and post-fixed in Karnovsky's fixative for at least 2 weeks. Transmission electron microscopy was performed in the region of the M2 subcortical fibers as they leave cortical layer VI and enter the corpus callosum. The samples were then post-fixed in 1% osmium tetroxide (EMS 19100) for 1 hr at room temperature, washed 3 times with ultrafiltered water, then en bloc stained for 2 hr at room temperature. Samples were then dehydrated in graded ethanol (50%, 75%, and 95%) for 15 min each at 4°C; the samples were then allowed to equilibrate to room temperature and were rinsed in 100% ethanol 2 times, followed by acetonitrile for 15 min. Samples were infiltrated with EMbed-812 resin (EMS 14120) mixed 1:1 with acetonitrile for 2 hr followed by 2:1 EMbed-812:acetonitrile for 2 hr. The samples were then placed into EMbed-812 for 2 hr, then placed into TAAB capsules filled with fresh resin, which were then placed into a 65°C oven overnight. Sections were taken between 75 and 90 nm on a Leica Ultracut S (Leica, Wetzlar, Germany) and mounted on Formvar/carbon coated slot grids (EMS FCF2010-Cu) or 100 mesh Cu grids (EMS FCF100-Cu). Grids were contrast stained for 30 s in 3.5% uranyl acetate in 50% acetone followed by staining in 0.2% lead citrate for 30 s. Samples were imaged using a JEOL JEM-1400 TEM at 120kV and images were collected using a Gatan Orius digital camera. With experimenters blinded to sample identity and condition, axons were analyzed for *g*-ratios calculated by dividing the axonal diameter by the corresponding axonal-plus-sheath diameter (diameter of axon/diameter of axon + myelin sheath) at 4000X using ImageJ software. For each animal, approximately 100 axons were scored. Statistics for *g*-ratios were calculated on a per animal basis.

IC₅₀ Testing

96 well plates (Corning Life Sciences, Corning, NY) were coated with 50 μL of PLL (Poly-L-Lysine, 10 $\mu\text{g}/\text{mL}$, Sigma-Aldrich, St. Louis, MO) for 30 min, and then rinsed 3 times with PBS, each rinse at least 5 min in duration. After the last rinse with PBS, the plates were stored in the incubator at 37°C for at least 3 hr. Cells were plated at concentration of 5000 cells/well in 100 μL of their respective medium. Triplicates for each concentration of MTX (diluted in cell medium appropriate for each cell line) from 10 mM of MTX to 10 pM (decreasing in concentration by an order of magnitude for every triplicate), were tested to best determine the IC₅₀ for each cell line. The cells were then incubated for 24 or 48 hr at 37°C. CellTiter-Glo reagent (Promega, G9243) was added at a 1:1 ratio (100 μL) and allowed to incubate for 10 min at room temperature before measuring luminescence using a plate reader (Thermoscientific Varioskan LUX multimode microplate reader). Average luminescence for each cell line at every concentration of MTX tested was normalized to the controls (no MTX exposure (positive control) and no cells plated (negative control)). Using this procedure, it was possible to determine the extent of cell death for every concentration of MTX tested and extrapolate the concentration of MTX exposure leading to 50% cell death of each cell line.

Syngeneic Transplantation of OPCs

eGFP (C57BL/6-Tg(CAG-EGFP)1Osb/J) mice (The Jackson Laboratory) on a CD57/BL6 background were bred with CD1 mice to produce animals that were syngeneic with the juvenile MTX or PBS treated mice used in this study. P6-8 GFP⁺ mice were used to sort PDGFR α ⁺ cells by FACS from the frontal cortex (see above). Sorted GFP⁺/PDGFR α ⁺ cells were immediately stereotactically transplanted unilaterally into deep cortical M2/cingulum of the corpus callosum (A-P: +0.7 mm; M-L: 0.9 mm; D-V: -2.0 mm) of previously treated MTX or PBS animals at P63 (four weeks post-treatment). Cells were injected at a concentration of 20,000 cells/ μL . Cells were allowed to engraft for 10 days before animals were transcardially perfused (see above).

Behavioral analysis

CatWalk

To investigate the effect of juvenile chemotherapy exposure on motor output, the CatWalk gait analysis system (Noldus, Netherlands) was used. To ensure consistent running, mice were acclimated to handling for several weeks before recording, and all tests were run in a dark room. Animals were tested four weeks (P63) after the cessation of the chemotherapy treatment paradigm previously described. No behavioral training on the CatWalk apparatus was performed. Behavioral testing was performed during the light cycle in a dark room with red light. Four successful runs (with success being characterized by variation under 60%, lasting no more than 5 s, and consistent movement) were processed with the CatWalk XT 9.0 software.

Our previous work suggests that swing speed, as a sensitive measure of motor system function, is selectively altered if myelination is affected within the premotor circuit. We did not expect to see a difference in stride length. In this study, only the following parameters were analyzed:

Swing speed: the speed (cm/s) of the paw during limb swinging. Swing speed was calculated as the average of the left and right forepaw swing speeds.

Stride length: the distance (cm) between successive placements of the same paw. Calculation of stride length is based on the X-coordinates of the center of the paw print of two consecutive placements of the same paw during maximum contact of the paw with the glass floor.

Open Field test

Social anxiety was analyzed using a modified version of the open field test that focused on an animal's willingness to explore objects placed in the center of an open field. All mice were exposed to the same MTX/PBS paradigm at P21-35 as described above. Animals were handled at P62 for 10 min. After handling, the mice were placed in the experimental chamber to acclimate for 20 min. The experimental chamber was 61cm x 61cm x 61cm made of opaque Plexiglas. A camera was mounted 115 cm above the chamber to record the animal's behavior. The test was conducted during the animal's light phase, in a dark room with only red light.

On the day of testing (P63) the mice were handled for two min, and then placed in the experimental chamber with two identical Lego objects (of approx. 5 cm in height). The mouse was allowed to explore the arena for 5 min. After the testing was completed the mice were weighed, as a measure of health, to allow the groups to be compared. The camera footage was then analyzed (using CowLog analysis software). The animal's willingness to explore the center of the arena with the objects was assessed.

Novel Object Recognition Test

Cognition was analyzed using a modified version of the novel object recognition task (NORT) that focused on the attentional component of the task. The test was modified so that the duration between the training and testing phase was shortened, this was to ensure that the test placed a greater cognitive load on short-term memory, attention and frontal lobe function rather than long-term memory and hippocampal function. All mice were exposed to the same MTX/PBS paradigm at P21-35 as described above. Animals were handled daily for the week leading up to the test for 2 min. After handling, the mice were then placed in the experimental chamber on P62 or P202 to acclimatize for 20 min prior to testing on P63 or P203, respectively. The set up consisted of an opaque Plexiglas experimental chamber 61cm x 61cm x 61cm, and a camera mounted 115 cm above the chamber. The test was conducted during the animal's light phase, in a dark room illuminated with only red light.

On the day of testing (P63 or P203) the mice were handled for 2 min and then placed in the chamber to acclimate for 20 min before being returned to the home cage for another 5 min. Mice were then placed in the experimental chamber with two identical Lego objects (of approx. 5 cm). Each time the mouse was placed into the chamber, the mouse was facing the opaque wall, with the animal's tail in the direction of the objects. During the training phase, the mouse was allowed to explore the identical objects for 5 min. The mouse was once again returned to the home cage for 5 min and the experimental chamber and the objects were cleaned with 70% ethanol. During this time, one cleaned object from the sample phase was placed back into the experimental chamber along with a new Lego object (of approx. 5 cm) for the novel object phase. During the testing phase, the mouse was returned to the experimental chamber and allowed to explore for 10 min.

The objects used as novel and familiar were counterbalanced, as was the position of the novel object from trial to trial, animal to animal. All of the Lego objects used in the behavioral paradigm were piloted to ensure that there was no bias, or object preference for the animals. The camera footage was then analyzed (using CowLog analysis software), and any exploratory head gestured within 2 cm of the Lego object, including sniffing and biting were considered object investigation, but not sitting on the object, or casual touching of the object in passing (Leger et al., 2013). Only animals that explored the objects for a minimum of 20 s for P63 or 10 s for P203 were included in the analysis. After the testing was completed the mice were weighed, as a measure of health, to allow the groups to be compared. The Recognition Ratio was determined by taking the ratio of the amount of time spent investigating one object compared to the total time spent investigating both objects (i.e., time spent with Novel Object / (time spent with Novel Object + time spent with Familiar Object)).

Microfluidic qRT-PCR

Total RNA was extracted from immunopanned cells using the RNeasy Plus kit (QIAGEN) and cDNA synthesis performed using the High-Capacity RNA-to-cDNA Kit (Applied Biosystems) according to supplier protocols. We designed primers using NCBI primer blast software (<http://www.ncbi.nlm.nih.gov/tools/primer-blast/>) and selected primer pairs with least probability of amplifying

nonspecific products as predicted by NCBI primer blast. We tested the specificity of the primer pairs by PCR with rat and mouse whole-brain cDNA (prepared fresh), and examined PCR products by agarose gel electrophoresis. For microfluidic qRT-PCR, 1.25 µL of each cDNA sample was pre-amplified using 2.5 µL of 2x Taqman pre-amplification master mix (Applied Biosystems) and 1.25 µL of the primer pool (0.2 pmol each primer/µL). Pre-amplification was performed using a 10 min 95°C denaturation step and 14 cycles of 15 sec at 95°C and 4 min at 60°C. Reaction products were diluted 1:5 in TE Buffer (Teknova). Five microliters from a sample mix containing pre-amplified cDNA and amplification Master mix (20 mM MgCl₂, 10 mM dNTPs, FastStart Taq polymerase, DNA binding dye loading reagent, 50 × ROX, 20 × Evagreen) was loaded into each sample inlet of a 96.96 Dynamic Array chip (Fluidigm) and 5 µL from an assay mix containing DNA assay loading reagent, as well as forward and reverse primers (10 pmol/µL) was loaded into each detector inlet. The chip was then placed in the NanoFlexTM 4-IFC Controller (Fluidigm) for loading and mixing. After loading, the chip was processed in the BioMarkTM Real-Time PCR System (Fluidigm) using a cycling program of 10 min at 95°C followed by 40 cycles of 95°C for 15 sec and 60°C for 30 sec and 72°C for 30 sec. After completion of qPCR, a melting curve of amplified products was determined. Data were collected using BioMarkTM Data Collection Software 2.1.1 build 20090519.0926 (Fluidigm) as the cycle of quantification (Cq), where the fluorescence signal of amplified DNA intersected with background noise. Data were corrected for differences in input RNA using the geometric mean of the reference gene *Rplp0*. Data preprocessing and analysis was completed using Fluidigm Melting Curve Analysis Software 1.1.0 build 20100514.1234 (Fluidigm) and Real-time PCR Analysis Software 2.1.1 build 20090521.1135 (Fluidigm) to determine valid PCR reactions. Invalid reactions were removed from later analysis. All primer sequences for rat and mouse were used previously (Liddelow et al., 2017; see Table S2).

Standard qRT-PCR

Total RNA was extracted and cDNA synthesized as above. Quantitative RT-PCR was run using 2 µL cDNA and SYBR green chemistry (Applied Biosystems/ThermoFisher Scientific) using supplier protocol and a cycling program of 2 min at 95°C followed by 40 cycles of 95°C for 3 sec and 60°C for 30 sec on a Mastercycler epgradient S (Eppendorf). After completion of qPCR, a melting curve of amplified products was determined. Data were collected using a Mastercycler ep realplex v2.2 (Eppendorf). All primer sequences for rat and mouse were used previously (Liddelow et al., 2017; see Table S2).

Depletion of microglia using PLX5622

PLX5622, an inhibitor of colony-stimulating factor 1 receptor, was administered to mice *ad libitum* from P38-63. PLX5622 was provided by Plexxikon Inc. (Berkeley, CA) and formulated in AIN-76A standard chow with 1,200 mg of PLX5622 by Research Diets Inc. Animals then underwent behavioral testing using the NORT or perfusion for immunohistochemical analysis, transmission electron microscopy analysis, or RNAScope analysis as described above.

QUANTIFICATION AND STATISTICAL ANALYSIS

For fluorescent immunohistochemistry of mouse tissue, total number of PDGFR α^+ only, PDGFR α^+ /Olig1^{nuclear}, Olig1^{perinuclear}, CC1⁺, EdU⁺/PDGFR α^+ , CD68⁺/Iba1⁺, cleaved caspase-3⁺ cells were quantified by a blinded rater for all 5 frames/animal (taken at 200X). Cells were considered co-labeled when they co-localized on the same plane. The density of cells was determined by dividing the total number of cells quantified for each lineage by the total volume of the imaged frames (mm³). For transplantation of syngeneic PDGFR α^+ cells, 30–50 GFP⁺ cells/animal were counted in the corpus callosum and assessed for co-localization with PDGFR α^+ , PDGFR α^+ /Olig1⁺, and Olig1⁺. Only GFP⁺ cells distant from the needle tract and within the corpus callosum were quantified to avoid any confounding inflammatory effects of activated microglia in response to the needle stick injury.

All statistical analyses were conducted using GraphPad Prism statistical software, including Tests of Normality. For density of PDGFR α^+ with and without EdU, PDGFR α^+ /Olig1^{nuclear}, Olig1^{perinuclear}, CC1⁺, CD68⁺/Iba1⁺, cleaved caspase-3, corpus callosum volume measures, *g*-ratios, behavioral tests, and syngeneic transplantation of GFP⁺ cells group mean differences were assessed using unpaired, two-tailed Student's *t* tests. For microglia and astrocyte reactivity states 2-way ANOVA with post hoc analyses were used to assess main group differences. For analysis of the effect of PLX5622 chow on microglial and oligodendroglial cell densities and astrocyte reactivity, 2-way ANOVA plus Tukey post hoc analyses or 1-way ANOVA were performed. For assessment of Olig2 immunohistochemistry in human samples, paired *t* tests were used. For parametric data, ANOVAs were run with post hoc analyses. For nonparametric data, Mann-Whitney statistical tests were implemented. A level of *p* < 0.05 was used to designate significant differences.

DATA AND SOFTWARE AVAILABILITY

Data Resources

Raw data are available through Mendeley Data: <https://doi.org/10.17632/wjhdwcrct.1>.

Supplemental Figures

Cell

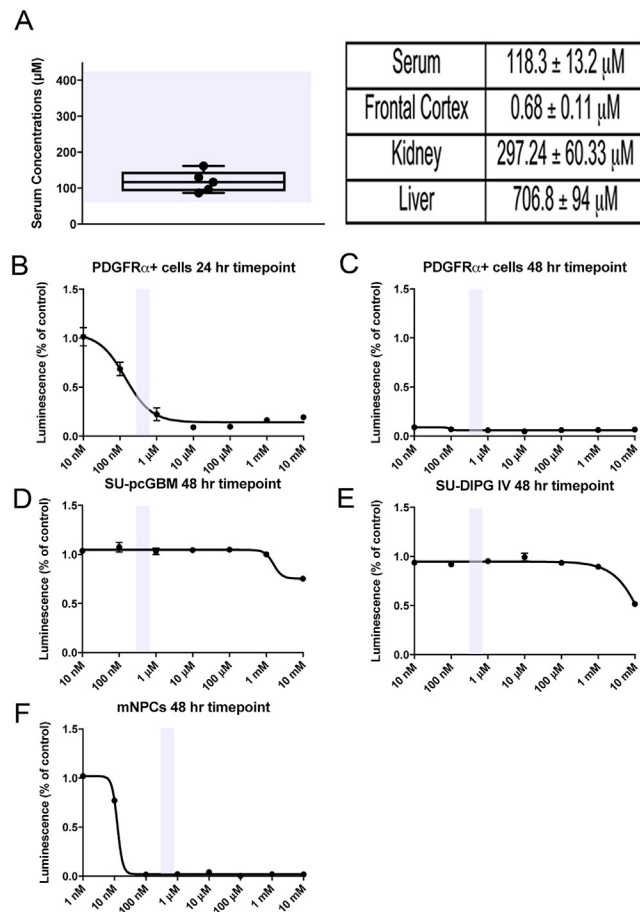


Figure S1. Methotrexate Tissue Concentrations and Cellular Sensitivities, Related to Figure 2

(A) Serum and tissue concentrations of methotrexate 30 min following a single 100 mg/kg i.p. dose of MTX, determined using LC-MS/MS. Dots represent individual mice ($n = 5$). The purple shaded region represents the range in serum concentrations detected in children following a single high-dose, 6-hr infusion of MTX (Bratid and Moe, 1978). Data shown as mean \pm SEM.

(B–F) MTX IC₅₀ curves for various cell populations. Purple bars represent MTX concentrations achieved in the mouse brain following a single 100 mg/kg i.p. injection of MTX. $n = 3$ wells for each data point.

(B and C) PDGFR α^+ cells were isolated from P6-8 mice using FACS and exposed to various MTX concentrations for 24 hr (B) or 48 hr (C). The 24-hr IC₅₀ for mouse PDGFR α^+ cells was 140.4 nM.

(D and E) 48-hr MTX IC₅₀ > 1 mM for patient-derived high-grade glioma cultures, pediatric cortical glioblastoma (SU-pcGBM, D) and diffuse intrinsic pontine glioma (SU-DIPG IV, E).

(F) 48-hr MTX IC₅₀ for neural precursor cells (NPC) derived from mouse brain is 12.4 nM.

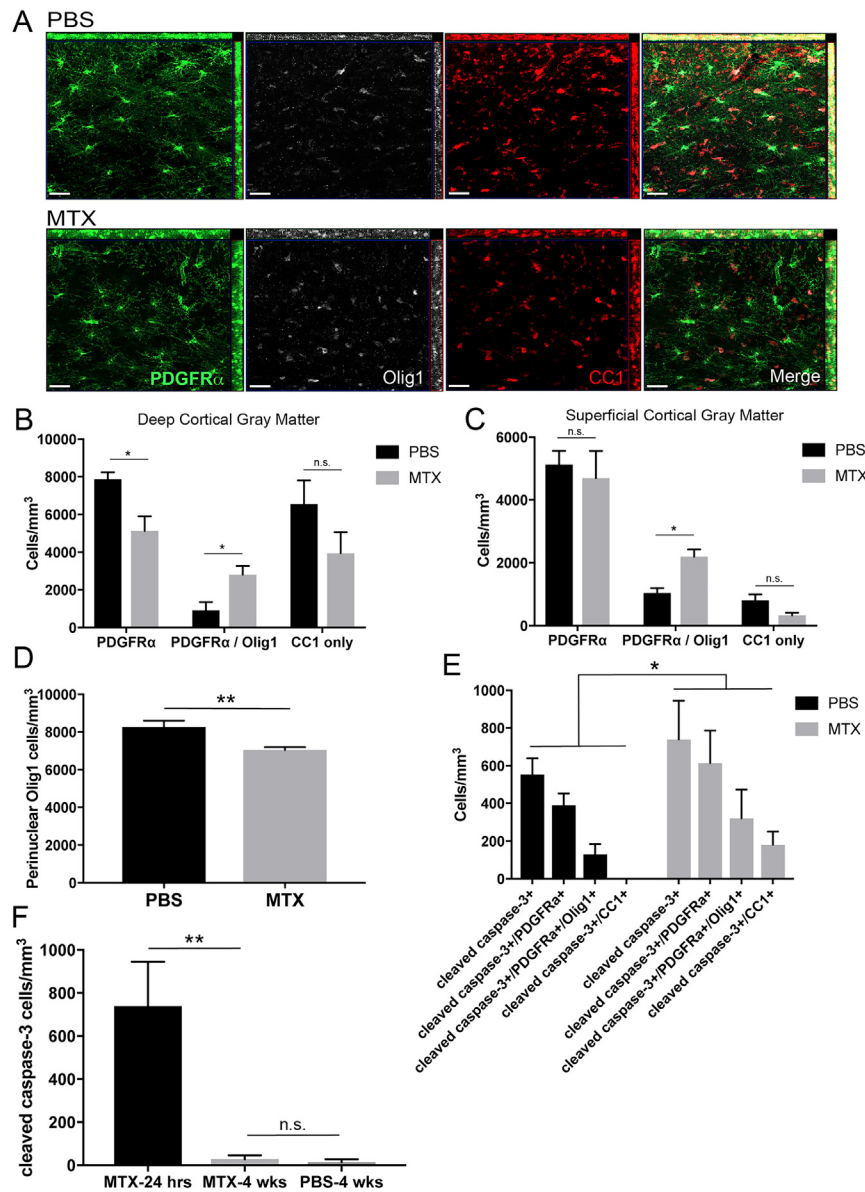


Figure S2. Oligodendroglial Lineage Dynamics and Cell Death after Methotrexate Exposure, Related to Figure 2

(A) Low-magnification confocal photomicrographs of PDGFR α ⁺ (green), Olig1⁺ (white), and CC1⁺ (red) cells in the corpus callosum of PBS- or MTX-exposed mice. Scale bar, 50 μ m.

(B) Similar to white matter, MTX induces a decrease in PDGFR α ⁺ OPCs ($p = 0.038$; $n = 4$ /group) and concomitant increase in PDGFR α ⁺/Olig1⁺ cells ($p = 0.025$; $n = 4$ /group) in the deep cortical gray matter of the premotor cortex without an increase in CC1⁺ mature oligodendrocytes ($n = 7$ /group; $p = 0.15$).

(C) Juvenile MTX treatment does not decrease the cell density of PDGFR α ⁺ OPCs ($p = 0.68$; $n = 4$ /group) or CC1⁺ mature oligodendrocytes ($p = 0.091$; $n = 7$ /group) in the superficial gray matter but does increase PDGFR α ⁺/Olig1⁺ cell density ($n = 4$ /group; $p = 0.016$).

(D) MTX ($n = 7$ mice) exposure decreases perinuclear Olig1⁺ cell density in the corpus callosum compared to PBS ($n = 8$ mice) treatment ($p = 0.0075$).

(E) Apoptotic cells as marked by cleaved caspase-3 without ("cleaved caspase-3") or with co-localization of PDGFR α , Olig1, or CC1 24 hr following a single i.p. injection of MTX ($n = 7$ mice) or PBS vehicle control ($n = 6$ mice) at P21 ($p = 0.0356$).

(F) Density of non-PDGFR α ⁺ cleaved caspase-3⁺ cells in the corpus callosum 24 hr following a single MTX injection at P21 ($n = 7$ mice) and four weeks following juvenile MTX ($n = 7$ mice) or PBS ($n = 8$ mice) injections at P21, 28, and 35 (MTX 24hr vs. MTX 4 wks, $p = 0.0048$). At 4 weeks, cleaved caspase-3 was not observed in any PDGFR α ⁺, Olig1⁺ nor CC1⁺ cells.

Data shown as mean \pm SEM, n.s. = $p > 0.05$, * $p < 0.05$, ** $p < 0.01$ by unpaired two-tailed Student's t test or two-way ANOVA (E).

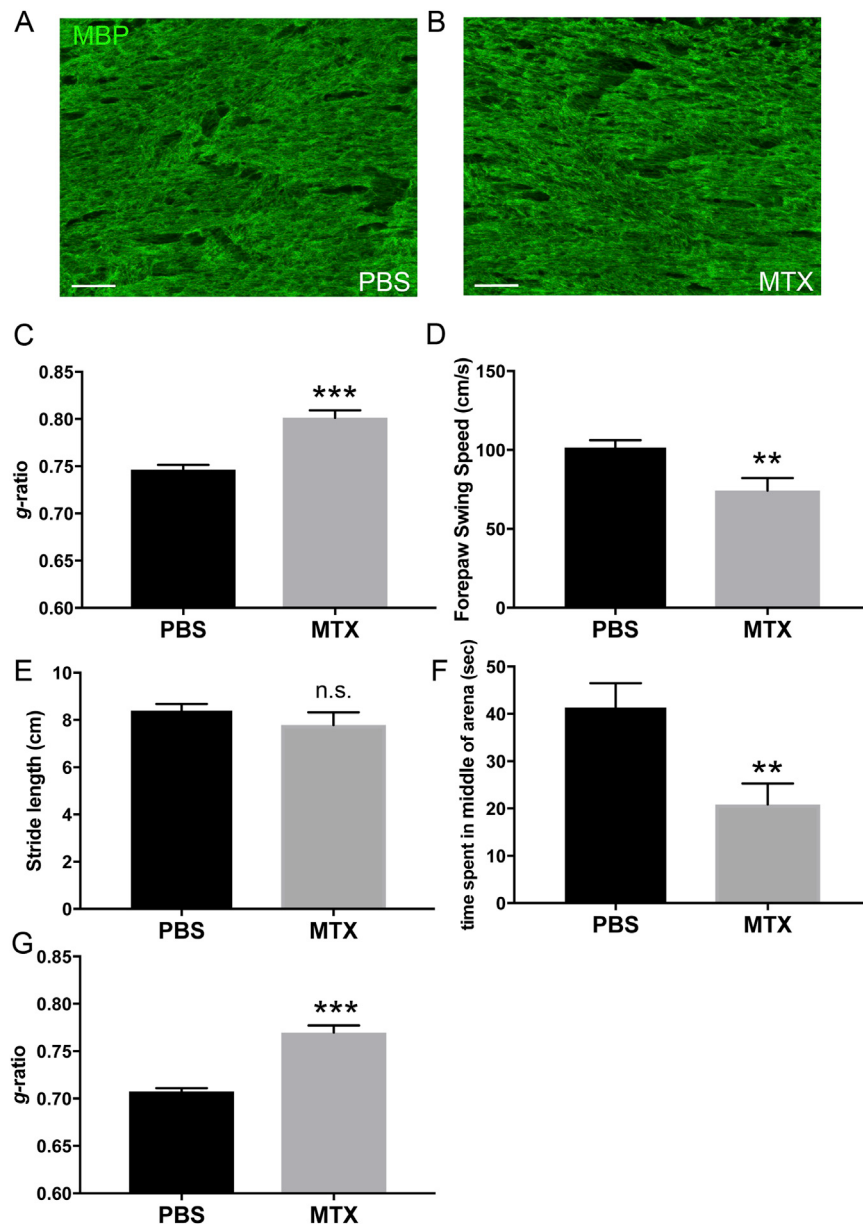


Figure S3. Myelin and Behavioral Changes after Methotrexate, Related to Figure 3

(A and B) High-magnification photomicrographs of myelin basic protein (MBP; green) in the corpus callosum of PBS- (A) and MTX- (B) exposed mice at P63. Scale bar, 20 μ m.

(C) Average g-ratio of premotor circuit axons as they enter the cingulum of the corpus callosum in P63 PBS (0.7465 ± 0.005 ; n = 5) and MTX (0.8014 ± 0.0079 ; n = 8) exposed mice four weeks following treatment ($p = 0.0003$).

(D and E) Catwalk gait analysis was used to assess motor performance in mice at P63 following PBS or MTX exposure. MTX-exposed mice exhibit decreases in forepaw swing speed (D; $p = 0.0067$) with no observed alterations to stride length (E; $p = 0.2986$; n = 9 mice PBS, n = 6 mice MTX).

(F) Anxiety following chemotherapy exposure was assessed using an open-field test at P63 ($p = 0.0082$; n = 12 mice PBS, n = 10 mice MTX).

(G) Average g-ratio of premotor circuit axons as they enter the cingulum of the corpus callosum in P203 PBS- (0.7073 ± 0.004 ; n = 4) and MTX- (0.7697 ± 0.007 ; n = 4) exposed mice 6 months following treatment ($p = 0.0003$).

Data shown as mean \pm SEM, n.s. = $p > 0.05$, ** $p < 0.01$, *** $p < 0.001$ by unpaired two-tailed Student's t test.

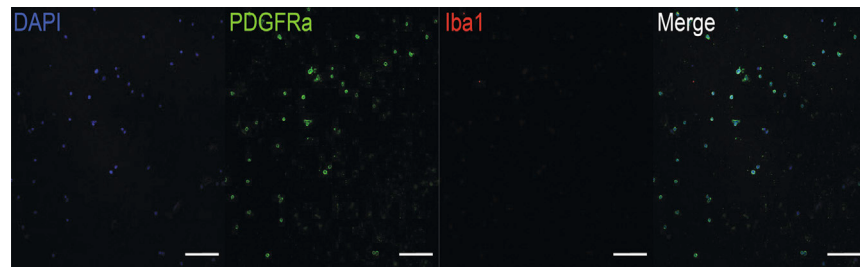


Figure S4. OPC Purity Validation for FACS Isolation Strategy, Related to Figure 4

Photomicrograph of cultured PDGFR α ⁺ cells (green) sorted by FACS. Sort purity for PDGFR α ⁺ cells is 98.03%, with very few Iba⁺ microglial cells (red). DAPI (blue); Scale bar, 50 μ m.

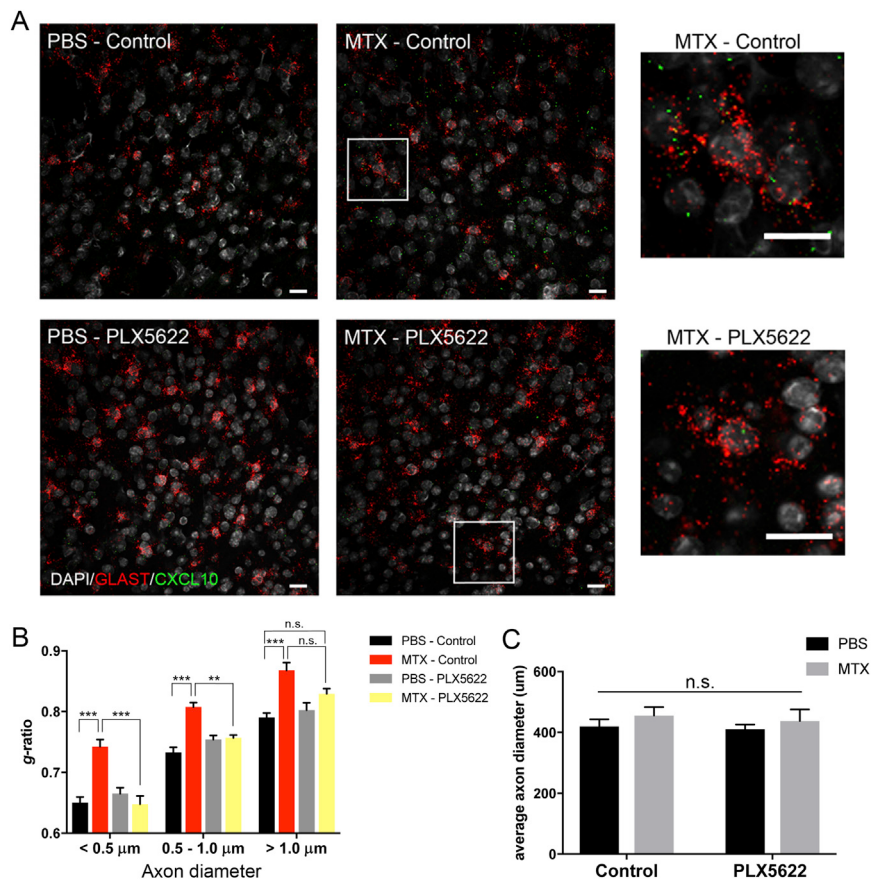


Figure S5. Astrocyte Reactivity and Myelinated Axon Microstructure following Methotrexate Exposure and Microglial Depletion, Related to Figure 7

(A) Confocal photomicrographs of *Cxcl10* puncta (green) in *Glast*⁺ astrocytes (red) in PBS- and MTX-exposed mice with and without PLX5622; Scale bar, 20 μ m.

(B) Microglial depletion (PLX5622) rescues myelin deficits in mice exposed to juvenile MTX in small ($< 0.5 \mu$ m; $p < 0.0001$) and medium (0.5μ m– 1.0μ m; $p = 0.0084$) caliber axons but not completely in large caliber axons ($> 1.0 \mu$ m; $p = 0.06$) compared to MTX-control mice. PBS-control n = 3 mice; MTX-control n = 3 mice; PBS-PLX5622 n = 5 mice; MTX-PLX5622 n = 3 mice.

(C) Average axon diameter in MTX and PBS mice with or without microglial depletion, measured at P63.

Data shown as mean \pm SEM, n.s. $p > 0.05$, ** $p < 0.01$, *** $p < 0.001$ by two-way ANOVA with Tukey post hoc testing.